

Anisotropy analysis for optimized gas production in Coalbed Methane reservoir, Bokaro field, India

Abir Banerjee (✉ Banerjee_Abir@ongc.co.in)

Oil and Natural Gas Corporation Limited, Bokaro, India

Rima Chatterjee

Indian Institute of Technology (Indian School of Mines), Dhanbad, India

Dip Kumar Singha

Banaras Hindu University, Varanasi, India

Research Article

Keywords: Anisotropy, Dewatering, Dispersion, Stress orientation, Resistivity Image

Posted Date: June 3rd, 2021

DOI: <https://doi.org/10.21203/rs.3.rs-582910/v1>

License: © ⓘ This work is licensed under a Creative Commons Attribution 4.0 International License.

[Read Full License](#)

Version of Record: A version of this preprint was published at Geophysical Prospecting on June 13th, 2022. See the published version at <https://doi.org/10.1111/1365-2478.13236>.

1 **Anisotropy analysis for optimized gas production in Coalbed Methane**
2 **reservoir, Bokaro field, India**

3 ¹**Abir Banerjee**, ²**Rima Chatterjee**, ³**Dip Kumar Singha**

4 1. Oil and Natural Gas Corporation Limited, Bokaro, Jharkhand-827001, India

5 2. Dept. of Applied Geophysics, IIT(ISM) Dhanbad, Jharkhand- 826004, India

6 3. Department of Geophysics, Banaras Hindu University, Varanasi, India

7 Corresponding Author email: Banerjee_Abir@ongc.co.in

8

9

10 Corresponding author: Abir Banerjee
11 Senior Geoscientist
12 Department of Well Logging
13 Oil and Natural Gas Corporation Limited, CBM Asset
14 Jharkhand-827001, India
15 Email: Banerjee_Abir@ongc.co.in

16

17

18

19

20

21

22

23

24 **Abstract**

25 The efficient production of Coalbed Methane (CBM) gas is facing challenges due to the larger
26 dewatering period from fracture connectivity to the aquifer zone. Also, commingled production
27 from well makes it more difficult to identify the coal seam-wise problem. Therefore, prior
28 knowledge of sub-surface fractures in coal seams is necessary to execute an accurate
29 simulation model for planning hydraulic fracturing treatment. This paper highlights the studies
30 in Bokaro CBM reservoir to mitigate challenges in few wells by characterizing anisotropy,
31 determining fast shear wave polarization angle, maximum horizontal stress direction, fracture
32 orientation, and analysis of low resistivity signature. Both the fast shear wave polarization
33 angle and fracture orientation in resistivity image are observed in the same direction (N26°-
34 35°E) in coal. The fast and slow shear slowness versus frequency plot concludes stress-induced
35 anisotropy resulting from fractures that are supported by resistivity image and drilling core.
36 Processing of the resistivity image log shows the maximum horizontal stress is along NE-SW
37 direction, as identified from drilling-induced fractures. The observation of low resistivity
38 signature with resistivity ranging from 0.4 to 0.8 ohm-m in few wells confirms the presence of
39 conducting minerals such as siderite and pyrite from the x-ray diffraction studies of sidewall
40 core. The present work guides in making production, drilling, and hydraulic fracturing design
41 strategies to better understand the fluid propagation for optimized CBM production and will
42 also help in future geomechanical studies.

43 **Keywords**

44 Anisotropy; Dewatering; Dispersion; Stress orientation; Resistivity Image

45 **Highlights**

- 46 • Anisotropy analysis and characterization in coalbed methane reservoir.

- 47 • Fractures, cleats and drilling-induced fractures identification from resistivity image log.
- 48 • Determination of maximum horizontal stress direction.
- 49 • Investigation of low resistivity signature from x-ray diffraction studies.
- 50 • Implication on the production process for CBM reservoir development.

51 **1. Introduction**

52 Coalbed methane (CBM) gas is becoming an alternate energy resource from the last decade in
53 exploration and consumption viewpoint. India is among the fifth largest producer and has
54 proven coal reserves in the world (Chatterjee et al. 2019). Exploration of CBM has many
55 challenges and needs proper planning and technologies for extracting methane gas (Paschin
56 and Groshong 1998; Bell and Bachu 2003). Coal has low permeability and the methane gas
57 production increases significantly with presence of naturally occurring fractures, cleats and
58 joints in imbedding sandstone and shale (Pitman et al. 2003; Chatterjee and Paul 2013).
59 However, primary permeability from natural fractures and cleats are not sufficient for the
60 production process, therefore hydraulic fracturing (HF) treatment in a coal seam is necessary to
61 create fractures for secondary permeability.

62 Anisotropy is an occurrence where the physical properties vary directionally in a medium.
63 Anisotropy can be two types: one is the intrinsic type due to the preferred mineral or grain
64 deposition as platy nature of thin isotropic layer and another is stress-induced anisotropy
65 appeared from initiation of fracture alignment (Wang 2002). The physical properties vary in
66 the horizontal or vertical plane with the borehole axis, it is known as Vertical Transverse
67 Isotropy (VTI), observed in shale or thinly bedded intervals (Cheng and Cheng 1996; Wang
68 2002). Pore structure, fabric, and stress are the concern of anisotropy. Coal matrix deformation
69 is related to the pore structure and fabric coal resulting from CBM gas adsorption/desorption.

70 The presence of opening mode fractures; face and butt cleats in coal is connected to stress-
71 induced anisotropy. Stress-induced anisotropy is derived from the S-wave velocities using
72 advanced sonic logging data indicates azimuthal anisotropy or horizontal transverse isotropy
73 (HTI) due to the variation of physical properties in the azimuthal direction around the wellbore
74 (Stevens and Day 1986; Cheng and Cheng 1996). The anisotropy mechanisms can be
75 distinguished and characterized through radial acoustic dispersion analysis (Plona et al. 2000;
76 Moreno et al. 2013).

77 In the petroleum industry, the anisotropy results are widely used for the optimization of
78 reservoir drainage, fault, and fracture detection and characterization in open hole, to forecast
79 borehole instability, design well, and evaluate well completion process for optimizing gas
80 production (Klimentos 2003; Franco et al. 2005). Properties of each compressional (P), shear
81 (S), and Stoneley (St) wave are affected by anisotropy in the formation. S-wave is influenced
82 by azimuthal anisotropy, St-wave responds to VTI anisotropy is established but P-wave is least
83 affected by anisotropy (Hornby et al. 1999; Sun et al. 2003). The dipole flexural S-mode is
84 affected and it gives erroneous results due to borehole failure or breakouts in an elliptical
85 borehole (Grandi et al. 2003). During data processing, the higher relative dip angle between the
86 borehole axis and formation beds is necessary to be considered (Tang and Patterson 2005; De
87 and Schmitt 2005).

88 Analysis of stress-dependent coal anisotropy is conducted for studying and determining the gas
89 flow and directional permeability in coal (Feng et al. 2019). Unconventional energy sources
90 like CBM, the anisotropy analysis is performed in the characterization of fractures and
91 determination of stress direction for well designing and estimating the permeable direction for
92 CBM reservoir simulation (Hower 2003; Feng et al. 2019). The occurrence of azimuthal
93 anisotropy from fractures in coal is established using seismic data was shown by many authors

94 (De et al. 1998; Gray et al. 2002; Vetri et al. 2003). Processing of cross multipole array
95 acoustics log data is required to know the dispersion characteristics of S-waves with frequency
96 for its identification of stress-induced and intrinsic anisotropy. Stress direction is required for
97 geomechanical application, oriented perforation, and effective fracturing in objective
98 formations (Fletcher et al. 1996; Todorovic-Marinic et al. 2004).

99 In a previous study on west Bokaro Coalfield (CF), the resistivity image log has identified the
100 Breakouts (BOs) oriented along N60°W and drilling-induced fractures (DIFs) oriented along
101 N15°E to N35°E, that are an important indicator of minimum (S_h) and maximum (S_H)
102 horizontal stress direction (Paul et al. 2017). But, in this CF, anisotropy analysis and its
103 characterization were not performed using sonic log, and the literature survey has not
104 mentioned the presence of a low resistivity signature (LRS). The objectives of this study are (a)
105 to analyze and characterize anisotropy using advanced sonic log, (b) to determine stress
106 direction and fracture orientations in coal seams, (c) to analyze the presence of the LRS in few
107 wells, and (d) to address the outcome of this work in assisting future planning for optimized
108 CBM production.

109 **2. Study Area**

110 The Bokaro district in the Jharkhand state of eastern India is a part of Damodar valley CF.
111 Lugu hill separates Bokaro CF into east and west. West and east Bokaro CF extend over an
112 area of 180 km² and 208 km², respectively (Banerjee and Chatterjee 2021). The Bokaro CF
113 comprising of Gondwana sediments, with dimensions 64 km x 12 km (Varma et al. 2014). The
114 study area of west and east Bokaro CF is shown in the geological map with wells (W-2 to W-4
115 and A-1 to A-4) in figure 1 (Banerjee and Chatterjee 2021). Mahadeva, Panchet, Raniganj,
116 Barren, Barakar, and Talchir are the geological formation in this CF in order from the top. The
117 coal deposits are found in the Barakar and Raniganj Formation. Drilling information have

118 reported the presence of 13 coal seams numbered as Seam “XIII to I” in order of descent in
119 Barakar formation in west CF with thickness of 300-550 meters (Murthy et al. 2016). The
120 present work is focused on 05 seams, namely “X, IX, VIII, VII+VII, V”. In east CF, major
121 seams are Karo, Bermo, Kargali Bottom, and Kargali Top (KT). The KT seam is focused on
122 east CF.

123 **Figure 1**

124 **3. Dataset**

125 Data of 07 wells named W-2, W-3, W-4, A-1, A-2, A-3, and A-4 are available in the study
126 area. All wells contain geophysical logs such as resistivity (RES), gamma-ray (GR), neutron
127 porosity (NEU) and density (DEN). Additionally, resistivity image log in W-2 and W-4,
128 advanced sonic log in W-2, production data of W-2, W-3, and W-4, drilling core (356.0 m to
129 362.5 m) in W-2 and X-ray diffraction (XRD) studies of sidewall core (SWC) samples in A-1
130 are available. The lithologies such as coal, shale, and sandstone are identified based on the
131 geophysical well logs cut-off criteria (Banerjee and Chatterjee 2021). In coal seam, GR (30-80
132 API), RES (900-50000 ohm-m), DEN (1.45-1.8 g/cc), and NEU (45-65 %) are the range of
133 geophysical parameters. **Figure 2** represents the geophysical log response of well W-2 and
134 objective coal seams are marked in the density log.

135 **Figure 2**

136 **4. Production Process and Problems**

137 The routine operational activities include the perforation of coal seam followed by hydraulic
138 fracturing (HF) treatment. Subsequently, the perforated and HF coal seams are pumped
139 continuously using an artificial pumping machine for dewatering and gas production.
140 Dewatering extracts the water volume from the coal seam to desorb the existing gas in an
141 adsorbed state by achieving the critical desorption pressure. Once the critical desorption

142 pressure is attained, the gas break occurs (Sun et al. 2017). Initially, only water is produced
143 without gas, but once gas breaks are attained, water production declines, and gas production
144 increases. A longer dewatering period is the challenge for cost optimization. The commingled
145 production from 05 seams with the period (days) shows larger dewatering (m^3/day) and smaller
146 discontinuous gas break (m^3/day) in W-2 and W-3, whereas in well W-4 no gas break is
147 observed (Figures 3a, 3b, 3c). The water and gas production in these 03 wells are different as
148 wells are drilled in different locations at different times but the recording interval of production
149 data is constant as shown in figure 3. Well W-2 is recorded from February 2019 to October
150 2019, but no major gas break is observed, hence the well was closed. Similarly, well W-3 is
151 recorded from 2017 to 2019 but the well was closed from January 2018 to January 2019 due to
152 well complication, after that it was again recorded with the observation of few discontinuous
153 gas breaks. The production data in well W-4 from September 2018 to June 2019 shows no gas
154 break and hence the well was closed. The average duration of production in these 03 CBM
155 wells was continued for 6-8 months as discontinuous/no gas breaks were observed.

156 **Figure 3**

157 **5. Mathematical Background**

158 The shear wave splitting phenomenon into fast and slow S-wave represents anisotropy in the
159 formation. Let us consider a multi-source and multi-receiver system where S-wave splitting
160 occurs. The splitting of the S-wave may or may not coincide with the natural coordinate system
161 (Crampin 1981; Thomsen 1988). In figure 4, S1 and S2 are the directions, and v_1 and v_2 are
162 the velocities of fast and slow S-wave in multiple sources and receiver systems. $S_a(t)$ and $S(t)$
163 are the source matrix in the acquisition and natural coordinate system. $S_R(t)$ and $S_T(T)$
164 represents the radial and transverse sources in the acquisition coordinate. The relationship

165 between these components are expressed in the form of the equation using vector rotation
 166 matrix $R(\theta)$:

$$167 \quad \begin{pmatrix} \cos \theta & \sin \theta \\ -\sin \theta & \cos \theta \end{pmatrix} \begin{pmatrix} S_R & 0 \\ 0 & S_T \end{pmatrix} = \begin{pmatrix} S_R \cos \theta & S_T \sin \theta \\ -S_R \sin \theta & S_T \cos \theta \end{pmatrix}, \quad (1)$$

$$168 \quad \text{Where } S_a(t) = \begin{pmatrix} S_R & 0 \\ 0 & S_T \end{pmatrix}, S(t) = \begin{pmatrix} S_R \cos \theta & S_T \sin \theta \\ -S_R \sin \theta & S_T \cos \theta \end{pmatrix} \text{ and } R(\theta) = \begin{pmatrix} \cos \theta & \sin \theta \\ -\sin \theta & \cos \theta \end{pmatrix}, \quad (2)$$

169 Similarly the reflected signal $V(t)$ is recorded in the acquisition coordinate, that is expressed as:

$$170 \quad R^{-1}(\theta) \bullet U(t) = V(t), \quad (3)$$

$$171 \quad \text{Where } V(t) = \begin{pmatrix} U_{11} \cos \theta & -U_{22} \sin \theta \\ U_{11} \sin \theta & U_{22} \cos \theta \end{pmatrix}, \text{ and } U(t) = \begin{pmatrix} U_{11} & 0 \\ 0 & U_{22} \end{pmatrix}, \text{ represents matrix in the natural}$$

172 coordinate system, U_{11} and U_{22} is the reflected signal along S1 and S2 direction.

173 The above equation from time domain to frequency domain is expressed as:

$$174 \quad R^{-1}(\theta) \bullet D(\omega) \bullet R(\theta) \bullet S_a(\omega) = V(\omega), \quad (4)$$

$$175 \quad \text{Where } D(\omega) = \begin{pmatrix} f_1(\omega)e^{-i\omega\delta_1} & 0 \\ 0 & f_2(\omega)e^{-i\omega\delta_2} \end{pmatrix} \text{ represent time-delay function of the fast and slow S-}$$

176 wave, δ_1 and δ_2 are the two-way travel time, and f_1 and f_2 are the filter function for the fast and

177 slow S-wave set for the attenuation, geometric spreading, and reflection coefficient.

178 By applying rotation in data matrix in both source and receiver coordinate, the output of rotated

179 data matrix is expressed as:

$$180 \quad D(\omega) \bullet S_a(\omega) = D(\omega) \bullet R^{-1}(\theta) \bullet D^{-1}(\omega) \bullet R(\theta) \bullet V(\omega) = W(\omega), \quad (5)$$

181 Considering $f_1(\omega) = f_2(\omega)$, the equation (5) is expressed as:

182
$$W(\omega) = \begin{pmatrix} w_{RR} & w_{RT} \\ w_{TR} & w_{TT} \end{pmatrix} = \begin{pmatrix} \cos^2 \theta + \sin^2 \theta e^{+i\omega\Delta} & \sin \theta \cos \theta - \sin \theta \cos \theta e^{+i\omega\Delta} \\ \sin \theta \cos \theta e^{-i\omega\Delta} - \sin \theta \cos \theta & \sin^2 \theta e^{-i\omega\Delta} + \cos^2 \theta \end{pmatrix} \bullet \begin{pmatrix} v_{RR} & v_{RT} \\ v_{TR} & v_{TT} \end{pmatrix}$$

183 , (6)

184 Where in W_{RT} and V_{RT} , R represents receiver direction and T represents transmitter direction,
 185 and $\Delta = 2z \left(\frac{1}{\beta_2} - \frac{1}{\beta_1} \right)$. The multiplication factor $e^{\pm i\omega\Delta}$ is the time shift factor from frequency to
 186 time domain.

187 Hence, equation (6) determines the angle (θ) between fast S-wave and acquisition line, and the
 188 time lag (Δ) between fast and slow S-wave, the acquisition matrix data $V(t)$ can be rotated into
 189 $W(t)$ for separating fast and slow S-wave. Parameters (θ, Δ) is computed by searching and
 190 rotating the input data by a set of range in angles and time, and the normalization of off-
 191 diagonal elements of the rotated matrix is expressed as:

192
$$\square e_{ij}(\theta, \Delta, t) \square_p = \left(\sum_{k=1}^N |w_{ij}(\theta, t + k\Delta t)|^p \right)^{\frac{1}{p}}, \quad (7)$$

193 Where N represents samples number in the search window and k and p are the integers.

194 **Figure 4**

195 **6. Methods**

196 The flowchart of integrated work to determine and characterize anisotropy, to understand sub-
 197 surface fracture system, stress direction, and to study core and production data using available
 198 data is presented in **figure 5**. The reason for larger dewatering and less/no gas break are
 199 analyzed from anisotropy analysis. LRS is observed below KT seam is concluded from the
 200 XRD study.

201 **Figure 5**

202 6.1 Anisotropy analysis

203 The advanced sonic tool has two sets of 8 acoustically isolated orthogonal receivers and two
204 sets of acoustically isolated orthogonal transmitters (Harrison et al. 1990; Brie et al. 1997).
205 Each receiver set receives either inline or cross-line (orthogonal) waveform for one transmitter
206 signal. Four waveform components, two inline and two cross-line dipoles are recorded for
207 anisotropy analysis (Bechham 1996; Walls et al. 1996). Alford rotation is applied to the
208 waveform to establish the orientation of fast and slow S-waves (Alford 1986). The resulting
209 waveform is processed using a cross-correlation technique called semblance processing for
210 getting fast and slow S-wave slowness (Kimball and Marzetta 1986; Esmersey et al. 1994),
211 represented in black line shown in projection log from depth interval 407.0 - 427.0 m in well
212 W-2 (Figure 6) and its output is applied to obtain the fast S-wave polarization angle and energy
213 anisotropy.

214 **Figure 6**

215 In coal, fast and slow S-wave slowness varies from 130-170 us/ft and 130-160 us/ft
216 respectively. The anisotropy in coal seams is analyzed from three types of indicators: (a)
217 energy anisotropy, (b) travel time (TT) anisotropy, and (c) slowness (DTS) anisotropy. Energy
218 anisotropy is determined from the percentage of the cross-dipole components relative to all
219 four components, the minimum, and maximum cross line energy at each depth are calculated.
220 The strength of the anisotropy is measured from the difference of maximum with minimum
221 cross-energy (Vasquez 2016). The TT and DTS anisotropy are calculated from the differences
222 in travel time and slowness between fast and slow principle waveform. The TT is obtained
223 from first arrival picking of slowness waveform and DTS anisotropy is obtained by dividing
224 the slowness difference by averaging fast and slow S-slowness to obtain the percentage
225 difference (Vasquez 2016).

226

227 **6.2 S-wave dispersion analysis**

228 Acoustic anisotropy is recognized from waveform components processing results but the cause
229 for anisotropy in the formation cannot be determined. To determine the cause, slowness vs.
230 frequency dispersion is obtained to extract the information. Four types of acoustic anisotropy
231 mechanisms can be identified through radial acoustic dispersion analysis in the formation: (a)
232 Homogeneous isotropic (b) Inhomogeneous isotropic (c) Homogeneous anisotropic and (d)
233 Inhomogeneous anisotropic. The four types of mechanisms are shown in **figure 7** (Plona et al.
234 **2000**; Moreno et al. **2013**). No S-wave splitting occurs over frequency in a homogeneous
235 isotropic medium (**Figure 7a**). In an inhomogeneous isotropic medium, no S-wave splitting
236 occurs but slowness data are higher compared to the predictive model (**Figure 7b**). In a
237 homogeneous anisotropic medium, parallel splitting of fast and slow S-wave slowness is
238 observed; this mechanism is associated with intrinsic anisotropy: the layering of fractures
239 (**Figure 7c**). In inhomogeneous anisotropic medium splitting of fast and slow S-wave slowness
240 is associated with crossover (**Figure 7d**), associated with the stress-induced anisotropy around
241 the wellbore.

242

Figure 7

243 **6.3 Resistivity image analysis**

244 The resistivity image log acquired from a high-resolution resistivity tool in water-based mud is
245 checked to ensure quality and speed correction is applied to analyze logging tool response
246 while acquiring the data. Processed image generated is equalized and normalized to obtain
247 static and dynamic images of the sub-surface formations. The resistivity image of the wellbore
248 is represented in a color spectrum ranging from low to high resistivity value in a flat surface in
249 the clockwise (North-East-South-West-North) direction of the wellbore. In static images,

250 resistivity color spectrum remains constant with depth, whereas, in dynamic image, enhanced
251 resistivity image spectrum with depth is generated.

252 In the image log, drilling-induced fractures (DIFs) and borehole breakouts (BOs) are the
253 indicators of the present-day stress direction (Barton et al. 1998; Barton and Zoback 2002; Ali
254 et al. 2017). BOs corresponds to the S_h direction occurs due to low mud weight, is not observed
255 in this study whereas DIFs are observed as a thin vertical pair of line at 180° apart in image
256 log, correspond to the S_H direction which occurs due to high mud weight (Bell and Gough
257 1979; Trautwein-Bruns et al. 2010). Fractures are observed as a sinusoidal curve in the image
258 log. Cleats are the natural fractures present in coal seam observed as small vertical to sub-
259 vertical lines and transverse lines in image log due to regional tectonic stress and internal
260 tectonic stress (Paschin et al. 1991; Laubach et al. 1998; Pitman et al. 2003). Features such as
261 DIFs, fractures, cleats, and coal bed are identified along with its azimuth and dip magnitude are
262 obtained in five coal seams in well W-2 and W-4. The resistivity image log is processed to pick
263 the dip magnitude. The magnitude is calculated from the following formula:

$$264 \quad dip = \tan^{-1}\left(\frac{h}{d}\right), \quad (8)$$

265 Where h is the height of crest and trough in meters, d is the borehole diameter in meters.

266

267 **6.4 Low resistivity signatures (LRS) analysis**

268 LRS is observed below the KT coal seam, which is set as a marker in few wells in east Bokaro
269 CF. Conventional resistivity logs in wells A-1, A-2, A-3, and A-4 are correlated and LRS
270 signature was observed (Figure 8). Resistivity in the LRS zone ranges from 0.4-0.8 ohm-m. To
271 investigate the LRS, SWC was extracted in A-1 at depth 418.0 m and XRD studies were

272 conducted in the laboratory. Also, conducting fractures are observed in the resistivity image log
273 in well A-2 against the LRS.

274 **Figures 8**

275 **6.5 Error analysis**

276 Error analysis is the measure of accuracy that identifies and detects uncertainty in the result.
277 The error in degree is obtained from the difference in the observed and predicted magnitude of
278 fast S-wave polarization direction. Hence, the error is plotted with depth for seam “X, IX, VIII,
279 VI+VII, and V” (**Figures 9a, 9b, 9c, 9d, 9e**). The root mean square (RMS) technique is used to
280 estimate the error. RMS error of 05 coal seams is calculated from the square root of the sum of
281 standard deviation between observed and predicted magnitude in **figure 9**. Mathematically, the
282 equation of RMS error is defined as:

$$283 \quad RMS_error = \sqrt{\frac{\sum_{d=1}^n (x_{obs} - x_{pred})^2}{n}}, \quad (9)$$

284 where x_{obs} is the observed magnitude of fast S-wave direction, x_{pred} is the predicted model
285 magnitude of fast S-wave direction, d is the depth points considered for calculation from 1 to n
286 in each seam.

287 **Figures 9**

288 **7. Results and Discussion**

289 Anisotropy is estimated from S-wave in well W-2 by applying the Alford rotation technique
290 and fast S-wave polarization direction is determined in 05 objective coal seams. The fast S-
291 wave polarization angle and fracture orientation are observed in the same direction in coal
292 seam. In coal, the average energy anisotropy varies from 10-80%, TT and DTS anisotropy
293 range from 0-20% and 0-15%. **Figure 10** represents seam-VIII that illustrates energy anisotropy

294 with maximum/minimum energy ranges from 50-65% / 10-30%, TT and DTS anisotropy varies
295 from 0-10% and 0-15%. Fast S-wave polarizes along N60°E and S60°W. The S-slowness
296 versus frequency dispersion cross-plot indicates stress-induced anisotropy in the wellbore at 19
297 depth points, intrinsic anisotropy at single depth point, and rest depth intervals are observed to
298 be homogeneous isotropic. In this work, three depth points in well W-2 marked as (a. at 342.0
299 m), (b. at 389.0 m), and (c. at 437.0 m) in fast and slow S-wave log illustrates three cases
300 respectively (Figure 11). The dispersion cross-plot of fast and slow S-waves are shown in red
301 and blue dots in figure 12. Figure 12a represents the depth at 342.0 m is observed to be a
302 homogeneous isotropic formation. Figure 12b represents the depth at 389.0 m in coal seam-V
303 which is in a stress-induced condition. Figure 12c represents the depth at 437.0 m that is
304 observed with intrinsic anisotropy in shale. Also, the correlation of anisotropic depths confirms
305 fractured in the resistivity image log.

Figure 10, 11 and 12

307 The S_H direction is estimated from DIFs in resistivity image from depth interval 618.0-650.0 m
308 is observed along NE-SW (N26°-35°E) in W-4 (Figure 13a). The DIF direction obtained in this
309 work matches well with the previous study as N15°E to N35°E by Paul et al. (2017). Figure
310 13b represents seam-V showing fractures, cleats, and coal bed in W-4 with its dip magnitude
311 and direction. Fractures are also observed in the drilling core at 356.0 m and 357.5 m, which
312 matches with the resistivity image log in W-2 (Figure 14). Cleats in coal orient in all
313 directions, but maximum cleats orientation tends toward NE-SW direction along S_H direction.
314 The dip direction of coal bed varies seam wise but dip magnitude ranges from 15°-25° in W-2
315 and 1°-10° in W-4. The dip orientation and magnitude of DIFs, fracture, cleats, and coal bed
316 are presented in stereonet plots for W-2 and W-4 (Figures 15a, 15b, 15c and 15d, 15e, 15f,
317 15g). The detailed analysis of dip magnitude and direction, fast S-wave polarization angle,
318 fracture orientation, cleats azimuth, and coal bed of coal seams “X, IX, VIII, VI+VII, and V” in

319 well W-2 and W-4 are tabulated in [table 1](#). The data in [table 1](#) are significant to establish a
320 seam-wise model. Error in fast S-wave polarization angle in seam “X, IX, VIII, VI+VII and V”
321 are 5.38° , 5.15° , 4.40° , 3.37° , and 4.81° respectively. The stress direction and fracture
322 orientation play an important role in designing HF treatment as HF fluid propagates along S_H
323 plane through fractures and connect to the aquifer that leads to larger dewatering. The
324 maximum fluid flow is along S_H direction, therefore, seam-wise planning for
325 perforation/oriented perforation for production is required instead of commingled production.
326 HF should be performed only in the least fractured coal seam and it should be avoided in a
327 highly fractured seam. Therefore, highly fractured coal production should be taken after
328 perforation, and if the gas production declines with time then HF should be executed. The
329 working guide to steer the trajectory for drilling horizontal/inclined well to pass through S_h
330 direction cutting maximum numbers of cleats and fractures that will enhance the natural flow
331 of fluids through increased connectivity between cleats and fractures. Additionally, stability of
332 horizontal/inclined wellbore increases if its trajectory passes through S_h direction.

333
334 The stress-induced anisotropic model in CBM reservoir will help in preparing the directional
335 mechanical earth model by integrating core and empirical geomechanical models. It will
336 establish a relationship in the directional variation of rock-mechanical properties in
337 understanding fracture extension and fluid propagation in coal seam during HF treatment. Lack
338 of core and geomechanical studies are the constraints for accurate design and implementation
339 of HF simulation model where rock-mechanical properties act as an important input parameter
340 for obtaining fracture parameters and volume of proppants requirement for pumping in a coal
341 seam. Previously, HF fluid movement could not be restricted within coal seams and has
342 propagated beyond the coal seams connecting the aquifer zone leading to a larger dewatering

343 period with less/no gas production. It occurs due to approximation and uncertainty in the
344 simulation model which impacts cost economics and delays in target achievement.

345
346 The XRD studies of SWC samples in LRS formation below KT seam in east Bokaro CF
347 confirms the deposition of conductive minerals such as siderite and pyrite in fractures from
348 (Figure 16). Identification of low resistivity signatures is acting as a marker below KT coal
349 seam helps in well correlation. The lower part of KT seam requires proper planning in HF
350 treatment. The corroboration of finding of fracture, fast S-wave direction, slowness frequency
351 dispersion cross-over or S_H direction between sonic, resistivity image, and core data suggests
352 the correctness of processing results. The robustness of the result will increase with the
353 presence of advanced sonic, resistivity image, and core data in other wells.

354 **Figure 13, 14, 15, 16, and Table 1**

355 **7. Conclusions**

356 The outcome of the study assist in optimized gas production in CBM reservoir from the
357 following conclusions:

358 (1) Anisotropy is analyzed from travel time delay of fast and slow shear wave. The fast shear
359 wave polarization direction, fracture orientation, and S_H direction matched well and are
360 observed along $N26^\circ-35^\circ E$ (NE-SW).

361 (2) Anisotropy associated with a coal seam is stress-induced due to the splitting phenomena in
362 slowness versus frequency plot. The stress-induced anisotropy is associated with the fractures
363 and cleats.

364 (3) Intrinsic anisotropy is caused due to parallel fractures in shale in Bokaro coalfield.

365 (4) The reason for the larger dewatering period in wells is due to the fracture extension through
366 HF treatment in the coal seam connecting the aquifer zone.

367 (5) This work provides vital information for drilling horizontal/inclined well, the production
368 flow path for oriented perforation, coal seam-wise model for operational and production
369 activities.

370 (6) Scope for future studies includes (i) geomechanical studies (ii) effective design for
371 hydraulic fracturing treatment (iii) fracture extension, and (iv) investigation of low resistivity
372 signature in the formation from geological and tectonic activities.

373

374 **Acknowledgment**

375 The authors are thankful to Oil and Natural Gas Corporation (ONGC) Limited for providing
376 permission to present this paper. The authors also wish to place on record the help and
377 guidance rendered by Mr. A.K Dwivedi (Ex-Director (Exploration), ONGC), and Mr. N.C.
378 Pandey (Ex-Director (T&FS), ONGC). We thank Mr. Shubham Dimri (technical engineer
379 Emerson-Paradigm), for the technical support in using Geolog software. No funding was
380 received in the preparation of this manuscript.

381 **Data Availability**

382 The data that support the finding of the result in this manuscript is available with the CBM,
383 Bokaro Asset of ONGC, India.

384

385 **References**

386 Alford, R. M. (1986). Shear Data in the Presence of Azimuthal Anisotropy: Dilley,
387 Texas. *Expanded Abstracts, 56th SEG Annual International Meeting and Exposition,*
388 *Houston, Texas, USA, November 2-6, Paper S9.6.*

- 389 Ali, M., Paul, S., & Chatterjee, R. (2017). Cleat Orientation from Ground Mapping and Image
390 Log Studies for In-Situ Stress Analysis: Coal Bed Methane Exploration in South
391 Karanpura Coalfield, India. *Energy & Fuels*, 31, 6812-6824.
- 392 Banerjee, A., & Chatterjee, R. (2021). A Methodology to Estimate Proximate and Gas Content
393 Saturation with Lithological Classification in Coalbed Methane Reservoir, Bokaro Field,
394 India. *Natural Resources Research*, 30, 2413-2429. [https://doi.org/10.1007/s11053-021-](https://doi.org/10.1007/s11053-021-09828-2)
395 [09828-2](https://doi.org/10.1007/s11053-021-09828-2)
- 396 Barton, C., Hickman, S., Morin, R., Zoback, M., & Benoit D. (1998). Reservoir-scale fracture
397 permeability in the Dixie Valley, Nevada, geotherma field. *SPE, ISRM*, 47371-27899.
398 <https://doi.org/10.2118/47371-MS>
- 399 Barton, C.A., & Zoback, M.D. (2002). Discrimination of natural fractures from drilling
400 induced wellbore failures in wellbore image data – implication of reservoir permeability.
401 *SPE Reservoir Evaluation and Engineering*, SPE 78599, 5(3), 249-254.
402 <https://doi.org/10.2118/78599-PA>
- 403 Beckham, W.E. (1996). Seismic Anisotropy and Natural Fractures from VSP and Borehole
404 Sonic Tools-A Field Study. *Geophysics*, 61(2), 456–466.
405 <http://dx.doi.org/10.1190/1.1443973>
- 406 Bell, J.S., & Bachu, S., 2003. In situ stress magnitude and orientation estimates for
407 Cretaceous coal-bearing strata beneath the plains area of central and southern Alberta.
408 *Bulletin of Canadian Petroleum Geology*, 51(1), 1–28.
409 <https://doi.org/10.2113/gscpgbull.51.1.1>
- 410 Bell, J.S., & Gough, D.I. (1979). Northeast-southwest compressive stress in Alberta evidence
411 from oil wells. *Earth and Planetary science letters*, 45(2), 475-482.
412 [https://doi.org/10.1016/0012-821X\(79\)90146-8](https://doi.org/10.1016/0012-821X(79)90146-8)

413 Brie, A., Kimball, C.V., Pabon, J., & Saiki, Y. (1997). Shear slowness determination from
414 dipole measurements. In 38 SPWLA Annual International Symposium, Houston, Texas,
415 Society of Professional Well Log Analysts, Paper F, 14.

416 Chatterjee, R., & Paul, S. (2013). Classification of Coal Seams for Coal Bed Methane
417 Exploitation in Central Part of Jharia Coalfield, India-A Statistical Approach. *Fuel*,
418 111, 20–29. <https://doi.org/10.1016/j.fuel.2013.04.007>

419 Chatterjee, R., Paul, S., & Pal, P.K. (2019). Relation between coalbed permeability and in-situ
420 stress magnitude for coalbed methane exploration in Jharia and Raniganj coalfields,
421 India. *The Leading Edge*, October, 800-807.

422 Cheng, N., Cheng, & C.H. (1996). Estimations of Formation Velocity, Permeability and
423 Shear-Wave Velocity Using Acoustic Logs. *Geophysics*, 61(2), 437–443.
424 <http://dx.doi.org/10.1190/1.1443971>.

425 Crampin, S., & Lowell, J. (1991). A decade of shear-wave splitting in the Earth's crust: what
426 does it mean? what use can we make of it? and what should we do next? *Geophysics*
427 *Journal International*, 107, 387-407.

428 De, G.S., & Schmitt, D.P., 2005. Issues with Shear-wave Azimuthal Anisotropy in Highly
429 Deviated Wells. In *Offshore Technology Conference, Houston, Texas, 2-5May, 2005*.
430 OTC-17647-MS. <http://dx.doi.org/10.4043/17647-MS>

431 De, G.S., Winterstein, D.F., Johnson, S.J., Higgs, W.G., & Xiao, H. (1998). Predicting natural
432 and induced fractures azimuths from shear wave anisotropy. *SPE Reservoir Evaluation &*
433 *Engineering*, August, 311-318. <https://doi.org/10.2118/50993-PA>

434 Esmersoy, C., Koster, K., Williams, M., Boyd, A., & Kane, M. (1994). Dipole shear anisotropy
435 logging. In Expanded Abstract, *SEG 64th Annual International Meeting*.

436 Feng, R., Chen, S., & Bryant, S. (2019). Investigation of Anisotropic Deformation
437 and Stress-Dependent Directional Permeability of Coalbed Methane Reservoirs. *Rock*
438 *Mechanics and Rock Engineering*, 1-15. <https://doi.org/10.1007/s00603-019-01932-3>.

439 Feng, R., Chen, S., Bryant, S., & Liu, J. (2019). Stress-dependent permeability measurement
440 techniques for unconventional gas reservoirs: Review, evaluation, and application. *Fuel*,
441 256, paper no. 115987.

442 Fletcher, P.A., Montgomery, C.T., & Ramos, G.G. (1996). Using fracturing as a technique for
443 controlling formation failure. *SPE 27899*, 11, 2. <https://doi.org/10.2118/27899-PA>

444 Franco, J.L.A., de la Torre, H.G., Ortiz, M.A.M. et al., (2005). Using Shear-Wave
445 Anisotropy To Optimize Reservoir Drainage And Improve Production In Low-
446 Permeability Formations in the North of Mexico, Presented at the SPE Annual
447 Conference and Technical Exhibition, Dallas, Texas; 9–12 October, 2005.
448 SPE96808-MS. <http://dx.doi.org/10.2118/96808-MS>

449 Grandi, S.K. et al., (2003). In Situ Stress Modeling at a Borehole - A Case Study, paper BH
450 1.4, Expanded Abstracts, Annual Meeting Technical Program, SEG, 297–300.

451 Gray, D., Roberts, G., & Head, K.J. 2002. Recent Advances in Determination of Fracture
452 Strike and Crack Density from P-Wave Seismic Data. *The Leading Edge*, 21(3), 280-285.
453 <https://doi.org/10.1190/1.1463778>

454 Harrison, A.R., Randall, C.J., Aron, J.B., Morris, C.F., Wignall, A.H., & Dworak, R.A. (1990).
455 Acquisition and analysis of sonic waveforms from a borehole monopole and dipole
456 source for compressional and shear speeds and their relation to rock mechanical
457 properties and surface seismic data. In paper SPE 20557, 65th SPE Annual Technical
458 Conference and Exhibition, New Orleans, September 23-26, 1990.

459 Hornby, B., Howie, J., & Ince, D. (1999). Anisotropy Correction for Deviated Well Sonic
460 Logs- Application to Seismic Well Tie, paper BH/RP 4.7. Expanded Abstracts,
461 Annual Meeting Technical Program, SEG. 1999; 112–115.

462 Hower, T.L. (2003). Coalbed Methane Reservoir Simulation: An Evolving Science. In paper
463 SPE 84424 presented at the SPE Annual Technical Conference and Exhibition, Denver,
464 Colorado, 5-8 October, 2003. <https://doi.org/10.2118/84424-MS>

465 Kimball, C.V., & Marzetta, T.L. (1986). Semblance processing of borehole acoustic array data.
466 *Geophysics*, 49(3), 274-281.

467 Klimentos, T. (2003). Shear-Wave Anisotropy Applications for Perforation Strategy and
468 Production Optimization in Oil Bearing Porous Sands. In paper LL. Trans., Annual
469 Logging Symposium, SPWLA, 1–12, 2003.

470 Laubach, S.E., Marrett, R.A., Olson, J.E., & Scott, A.R. (1998). Characteristics and origins of
471 coal cleat: A review. *International Journal of Coal Geology*, 35, 175–207.
472 [https://doi.org/10.1016/S0166-5162\(97\)00012-8](https://doi.org/10.1016/S0166-5162(97)00012-8).

473 Moreno, A., Rodriguez, G., Herrera, R.P., Perez, S., & Dip, G. (2013). Acoustic radial
474 Measurements Improve Fracture Characterization in Carbonate of South Mexico, Case
475 study: Cretaceous fractured carbonates in Navegate Field. *Society of Petroleum*
476 *Engineers*, Second South American Oil and Congress, SPE-WVS-73, Porlamar,
477 Margarita Island, Venezuela.

478 Pashin, J.C., & Groshong, Jr. R.H. (1998). Structural control of coalbed methane
479 production in Alabama. *International Journal of Coal Geology*, 38, 89–113.

480 Pashin, J.C., Ward, W.E.I.I., Winston, R.B. et al., (1991). Regional analysis of the Black
481 Creek-Cobb coalbed methane target interval Black Warrior basin, Alabama. *Alabama*
482 *Geological Survey Bulletin*, 145, 127.

483 Paul, S., Ali, M., & Chatterjee, R., (2017). Prediction of Compressional Wave Velocity Using
484 Regression and Neural Network Modeling and Estimation of Stress Orientation in Bokaro
485 Coalfield, India. *Pure and applied Geophysics*, 175(1), 375-388.

486 Pitman, J.K., Pashin, J.C., Hatch, J.R., & Goldhaber, M.B. (2003). Origin of minerals in
487 joint and cleat systems of the Pottsville Formation, Black Warrior basin, Alabama:
488 Implications for coalbed methane generation and production. *AAPG Bulletin*, 87(5),
489 713–731.

490 Plona, T., Sinha, B., Kane, M., & Vilorio, O. (2000). Using Acoustic Anisotropy, 40th Annual
491 SPWLA Logging Symposium; 2000.

492 Stevens, J.L., & Day, S.M. (1986). Shear Velocity Logging in Slow Formations Using the
493 Stoneley Wave. *Geophysics*, 51(1), 137–147. <http://dx.doi.org/10.1190/1.1442027> 22.

494 Sun, Y. et al., (2003). Effects of Stress-Induced Anisotropy on Monopole and Dipole
495 Logging. In paper RBG P1.2. Expanded Abstracts, Annual Meeting Technical
496 Program, SEG, 1282–1285.

497 Sun, Z., Li, X., Shi, J., Yu, P., Huang, L., Xia, J., et al. (2017). A semi-analytical model for
498 drainage and desorption area expansion during coal-bed methane production. *Fuel*, 204,
499 214–26. <https://doi.org/10.1016/j.fuel.2017.05.047>

500 Tang, X.M., & Patterson, D. (2005). Characterizing Seismic Anisotropy Using Cross-
501 Dipole Measurement in Deviated Wells. In paper BG 2.5, Expanded Abstracts,
502 Annual Meeting Technical Program, SEG, 372 – 375.

503 Thomsen, L. (1988). Reflection seismology in azimuthally anisotropic media. *Geophysics*, 53,
504 3, 304-313.

505 Todorovic-Marinic, D., Larson, D., Gray, D., Cheadle, S., Soule, G., & Zheng, Y. (2004).
506 Identifying vertical productive fractures in the Narraway gas field using the envelope of
507 the anisotropic gradient. *First Break*, 22, 10.

508 Trautwein-Bruns, U., Schulze, K.C., Becker, S., Kukla, P.A., & Urai, J.L. (2010). In situ stress
509 variations at the variscan deformation front - results from the deep Aachen geothermal
510 well. *Tectonophysics*, 493(1-2), 196-211. [https://doi.org/ 10.1016/j.tecto.2010.08.003](https://doi.org/10.1016/j.tecto.2010.08.003).

511 Varma, A.K., Hazra, B., Samad, S.K., Panda, S., & Mendhe, V.A. (2014). Methane sorption
512 dynamics and hydrocarbon generation of shale samples from West Bokaro and Raniganj
513 basins, India, *Journal of Natural Gas Science and Engineering*, 21, 1138-1147.

514 Vasquez, D. (2016). Optimize Full Waveform Sonic Processing. Paradigm Technical Session,
515 May 18th; 2016.

516 Vetri, L., Loinger, E., Gaiser, J., Grandi, A., & Lynn, H. (2003). 3D/4C Emilio: Azimuth
517 processing and anisotropy analysis in a fractured carbonate reservoir. *The Leading Edge*,
518 22(7), 675-679. <https://doi.org/10.1190/1.1599695>

519 Walls, J.D., Dvorkin, J., & Mavko, G. (1996). In-Situ Stress Magnitude and Azimuth from
520 Well Log Measurements. Final Report, Chicago, Illinois: Gas Research Institution,
521 Report GRI-95/0356, 1-147.

522 Wang, Z. (2002). Seismic Anisotropy in Sedimentary Rocks, Part 1 - A Single-Plug
523 Laboratory Method, Part 2 - Laboratory Data. *Geophysics*, 67(5), 1415–1440.

524

525

526
527
528
529
530
531
532

533 **Figure Captions**

534 **Figure 1.** The geological map of the Bokaro coalfield. (After Banerjee and Chatterjee, 2021).

535 **Figure 2.** Geophysical well logs (GR, RES, DEN, NEU) response from depth interval 115.0-
536 450.0 m in well W-2.

537 **Figure 3.** Dewatering (m³/day) and gas (m³/day) production profile versus period (days) in
538 wells (a) W-2 (b) W-3 (c) W-4.

539 **Figure 4.** Diagram representing S-wave splitting in multi-source and multi-receiver
540 acquisition.

541 **Figure 5.** Flowchart displaying the steps followed in the integrated work.

542 **Figure 6.** Slowness picking in black line of fast and slow S-wave from projection log after
543 semblance analysis in well W-2.

544 **Figure 7.** Classification of acoustic anisotropy from the fast shear (red line) and slow shear
545 (blue line) wave in slowness versus frequency plot. (a) Homogeneous isotropic (b)

546 Inhomogeneous isotropic (c) Homogeneous anisotropic (d) Inhomogeneous anisotropic
547 (redrawn after [Moreneo et al., 2013](#)).

548 **Figure 8.** Correlation of low resistivity signature (LRS) shown in the red rectangular box
549 below KT coal seam in the resistivity log of 04 wells (A-1, A-2, A-3, A-4).

550 **Figure 9.** The error with depth point in (a) Seam-X (b) Seam-IX (c) Seam-VIII (d) Seam-
551 VI+VII and (e) Seam-V.

552 **Figure 10.** Anisotropy analysis representing seam-VIII in well W-2 illustrates maximum and
553 minimum energy (%), DTS and TTS anisotropy (%), fast and 180° apart S-azimuth, resistivity
554 image with dip.

555 **Figure 11.** Fast and slow S-wave slowness (us/ft) from depth interval 115.0-450.0 m in well
556 W-2 and 03 points (a, b, c) marked in the log for anisotropy characterization.

557 **Figure 12.** Slowness vs. frequency dispersion plot of fast (red) and slow (blue) S-wave at three
558 depths: (a) Homogeneous isotropic formation at depth 342.0 m (b) Stress-induced fractured
559 coal seam-V with inhomogeneous anisotropic characteristics at depth 389.0 m (c) Intrinsic
560 anisotropy for homogeneous anisotropic formation at depth 437.0 m.

561 **Figure 13.** Static and dynamic resistivity image in well W-4 (a) represents DIFs with dip
562 magnitude and direction from 622.0-628.0 m, (b) represents dip magnitude and direction of
563 fractures and cleat in seam-V from depth interval 444.0-452.0 m.

564 **Figure 14.** Correlation of fractures at 356.0 m and 357.5 m between drilling core and
565 resistivity image log from depth 356.0 m to 362.5 m.

566 **Figure 15.** Stereonet plot representing dip magnitude and direction of 05 seams (V, VI+VII,
567 VIII, IX, X) in well W-2 (a) fracture (b) cleats (c) coal bed; and in well W-4 (d) fracture (e)
568 cleats (f) coal bed, (g) DIFs.

569 **Figure 16.** Cross-plot of intensity (cps) versus 2 θ (degree) from the XRD studies of SWC at
 570 418.0 m in well A-1 showing the presence of siderite and pyrite.

571

572

573

574

575

576

577 **Table caption**

578 **Table 1.** Comparison of dip and azimuth in 05 coal seams between different features in well
 579 W-2 and W-4.

Well: W-2					
Seam	Depth interval (m)	Fast S-wave direction	Fracture dip/azimuth	Cleats azimuth	Coal bed Dip/azimuth
X	235.0-242.5	N75°W	35°/N55°-85°E	E and NW-SE	30°/NE
IX	264.5-266.5	N15°W	50°/N45°E	Varies 360°	50°/NW
VIII	332.0-336.5	S60°W	35°/S35°-65°W	EW	35°/SW
VI+VII	385.0-390.5	N40°-65°E	30°/ N45°W- N45°E	NE-SW	30°/N30°E (Top) 35°/N25°W (Bottom)
V	413.0-420.7	N25°-60°E	25°/N20-25°E	NE and W	15°/N50°W (Top) 25°/N25°E (Bottom)

Well: W-4					
X	210.0-223.0	-	8°/E	NE-SW	8°/SW (Top) 5°/NE (Bottom)
IX	263.5-265.5	-	10°/N75°E	NE-SW and SE	10°/N (Top) 7°/N50°E (Bottom)
VIII	323.0-330.0	-	20°/E	NE-SW/NW-SE	6°/E
VI+VII	380.0-384.0	-	60°/N60°W	Varies 360°	8°/N50°E (Top) 8°/E (Bottom)
V	442.0-455.0	-	60°/NW	N15°E and SW	1°/N10°E (Top) 8°/N80°E (Bottom)

580

Figures

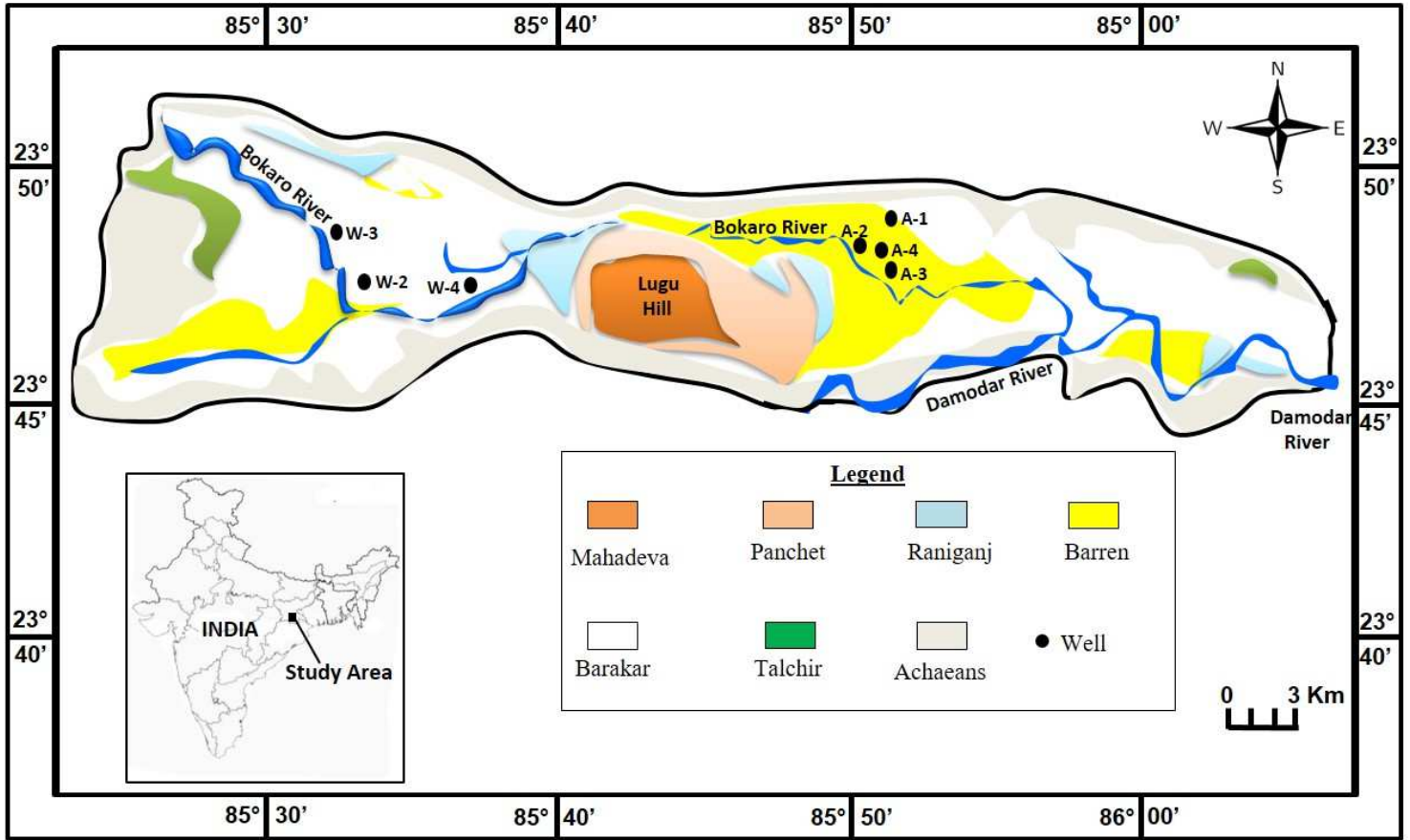


Figure 1

The geological map of the Bokaro coalfield. (After Banerjee and Chatterjee, 2021).

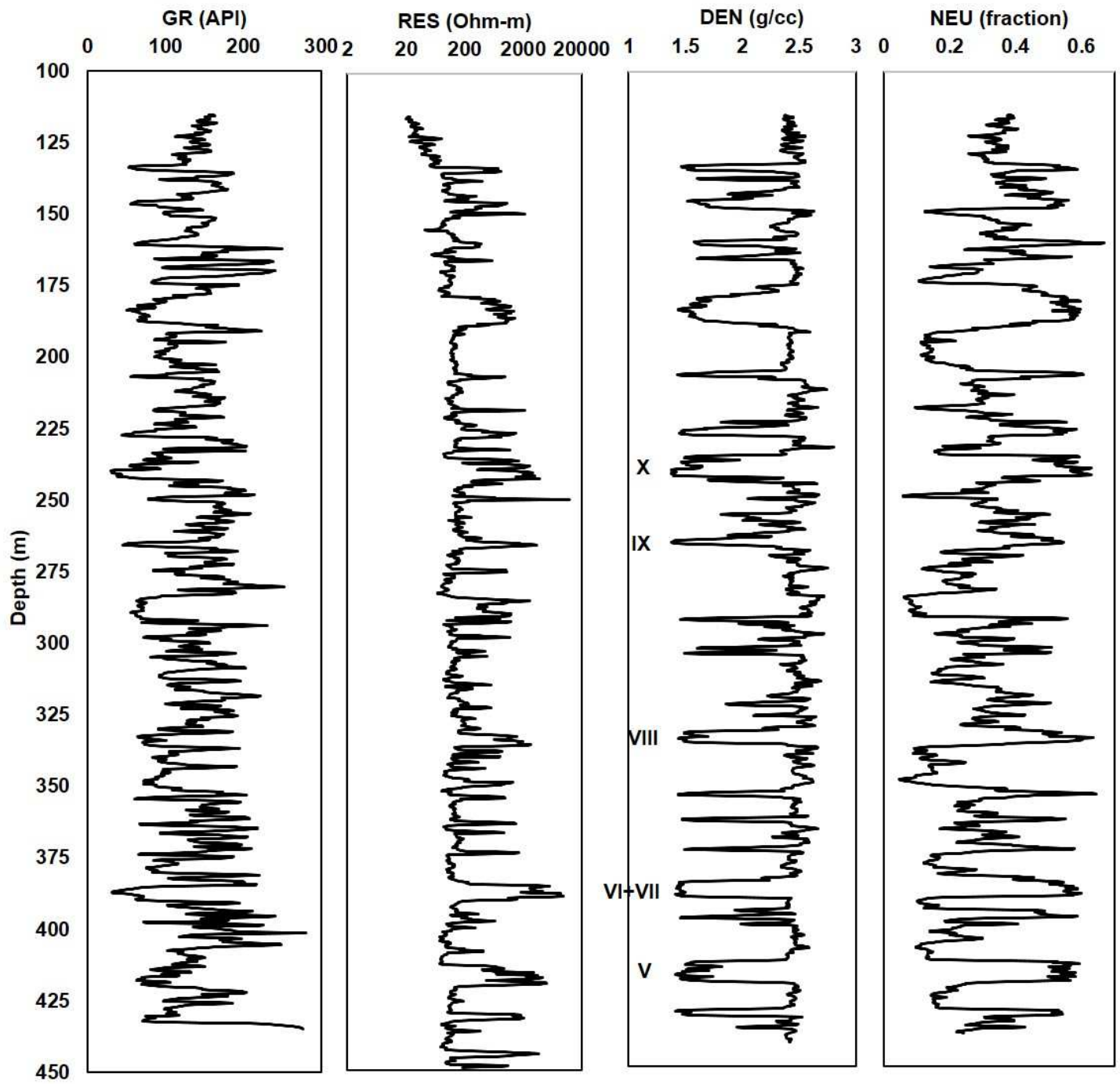


Figure 2

Geophysical well logs (GR, RES, DEN, NEU) response from depth interval 115.0-450.0 m in well W-2.

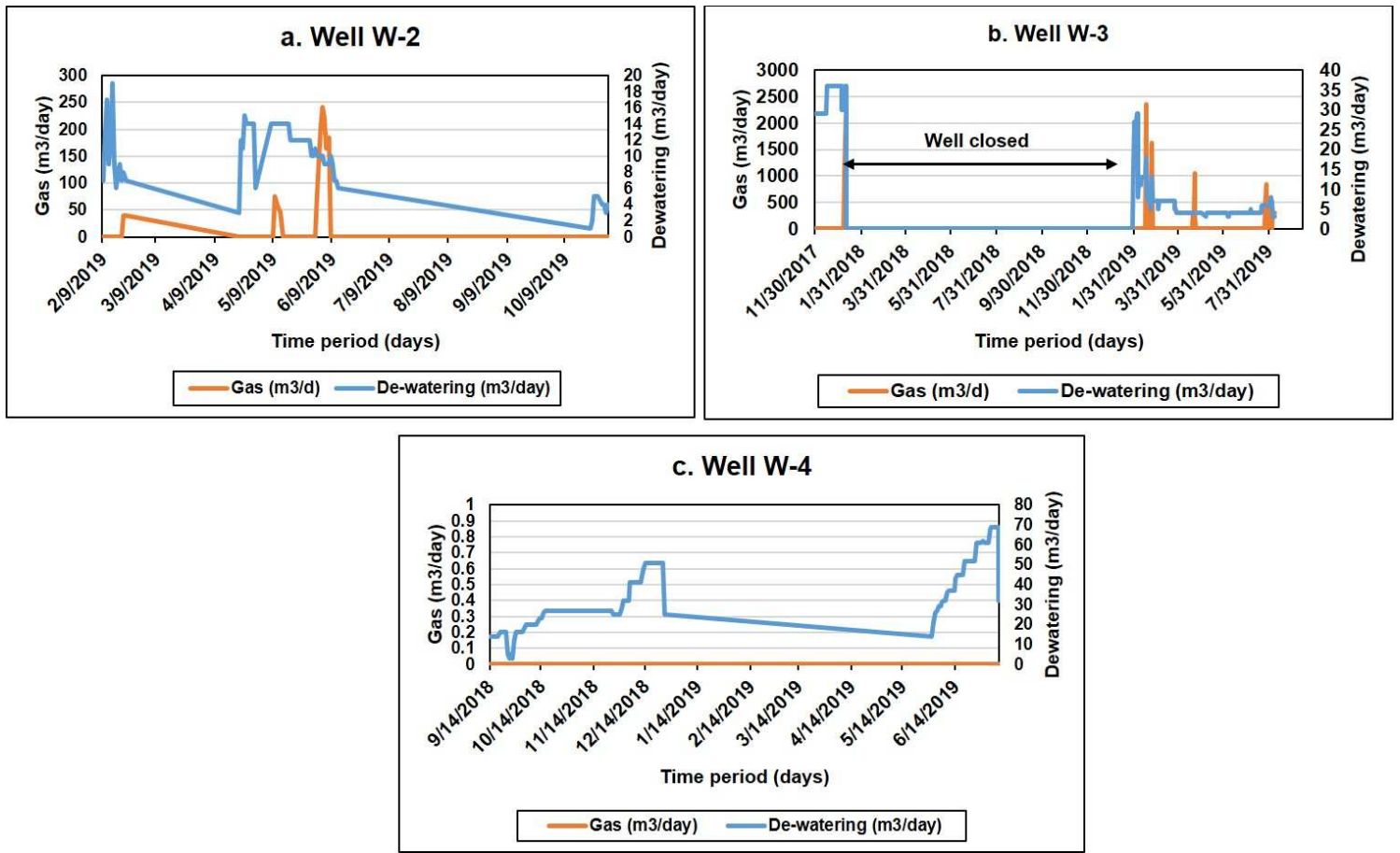


Figure 3

Dewatering (m³/day) and gas (m³/day) production profile versus period (days) in wells (a) W-2 (b) W-3 (c) W-4.

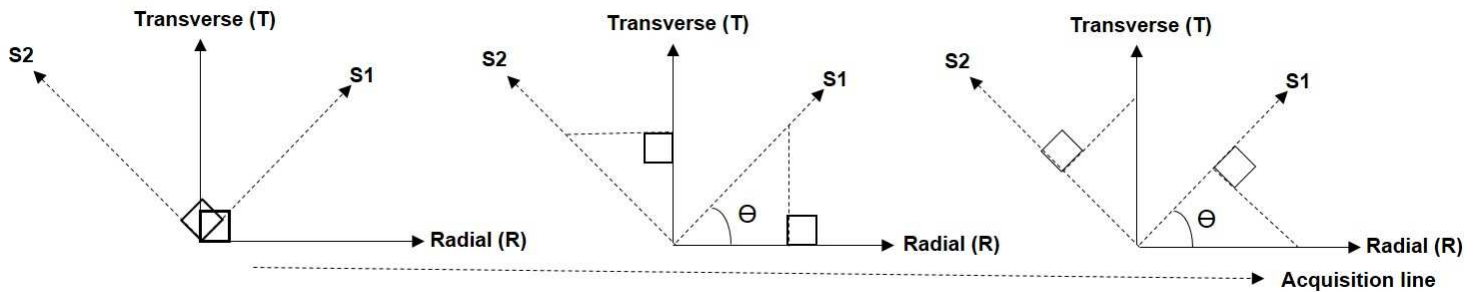


Figure 4

Diagram representing S-wave splitting in multi-source and multi-receiver acquisition.

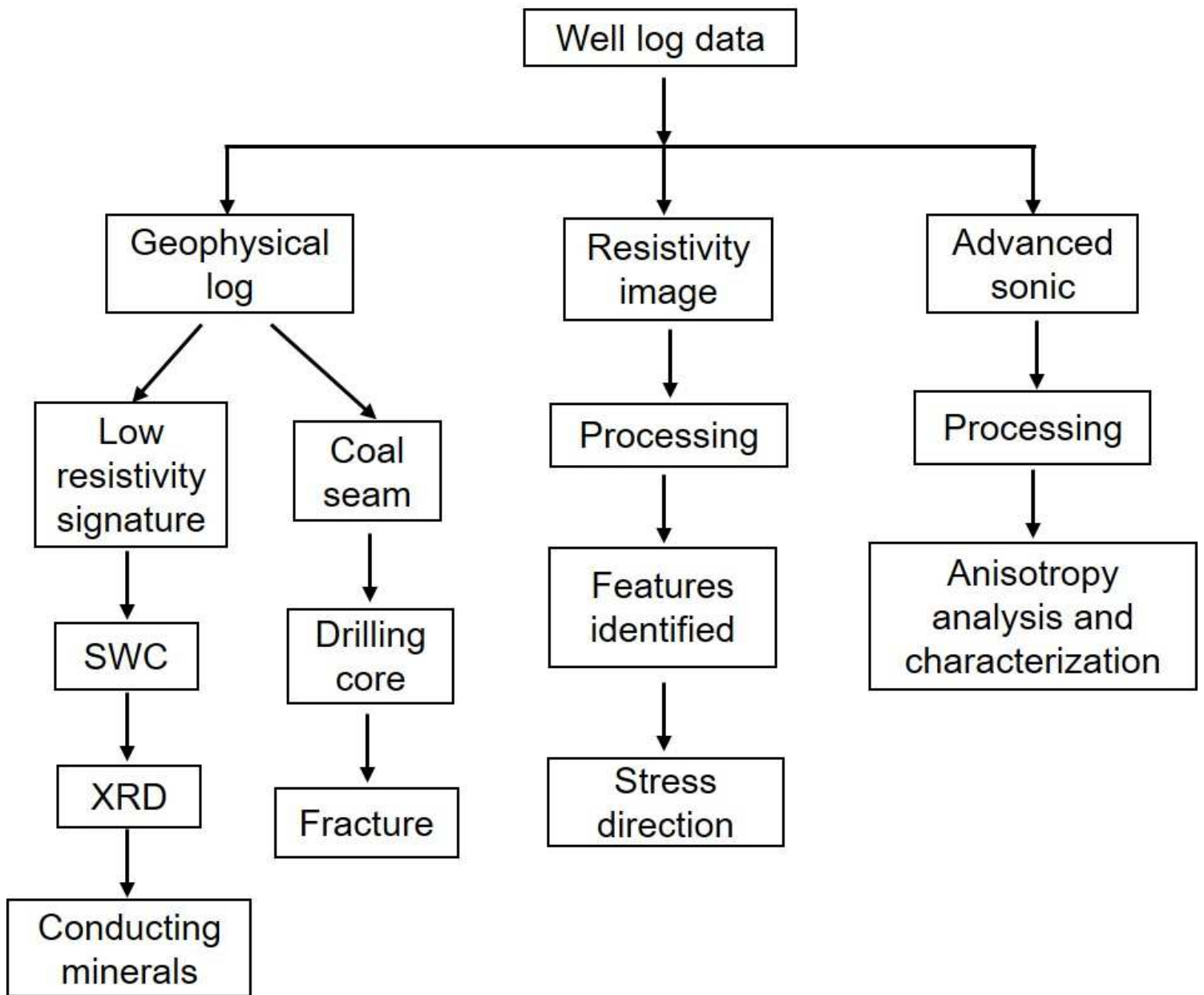


Figure 5

Flowchart displaying the steps followed in the integrated work.

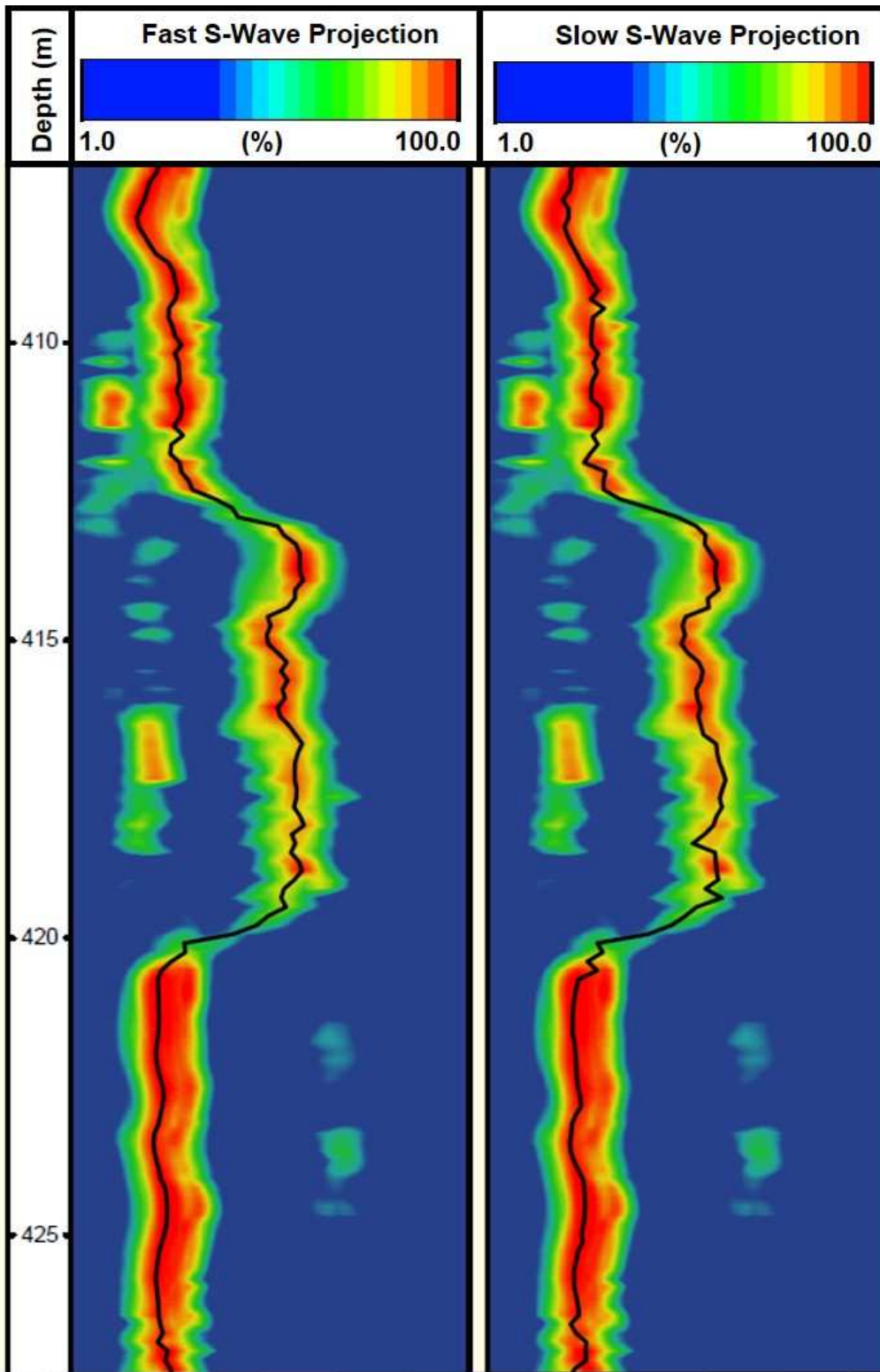


Figure 6

Slowness picking in black line of fast and slow S-wave from projection log after semblance analysis in well W-2.

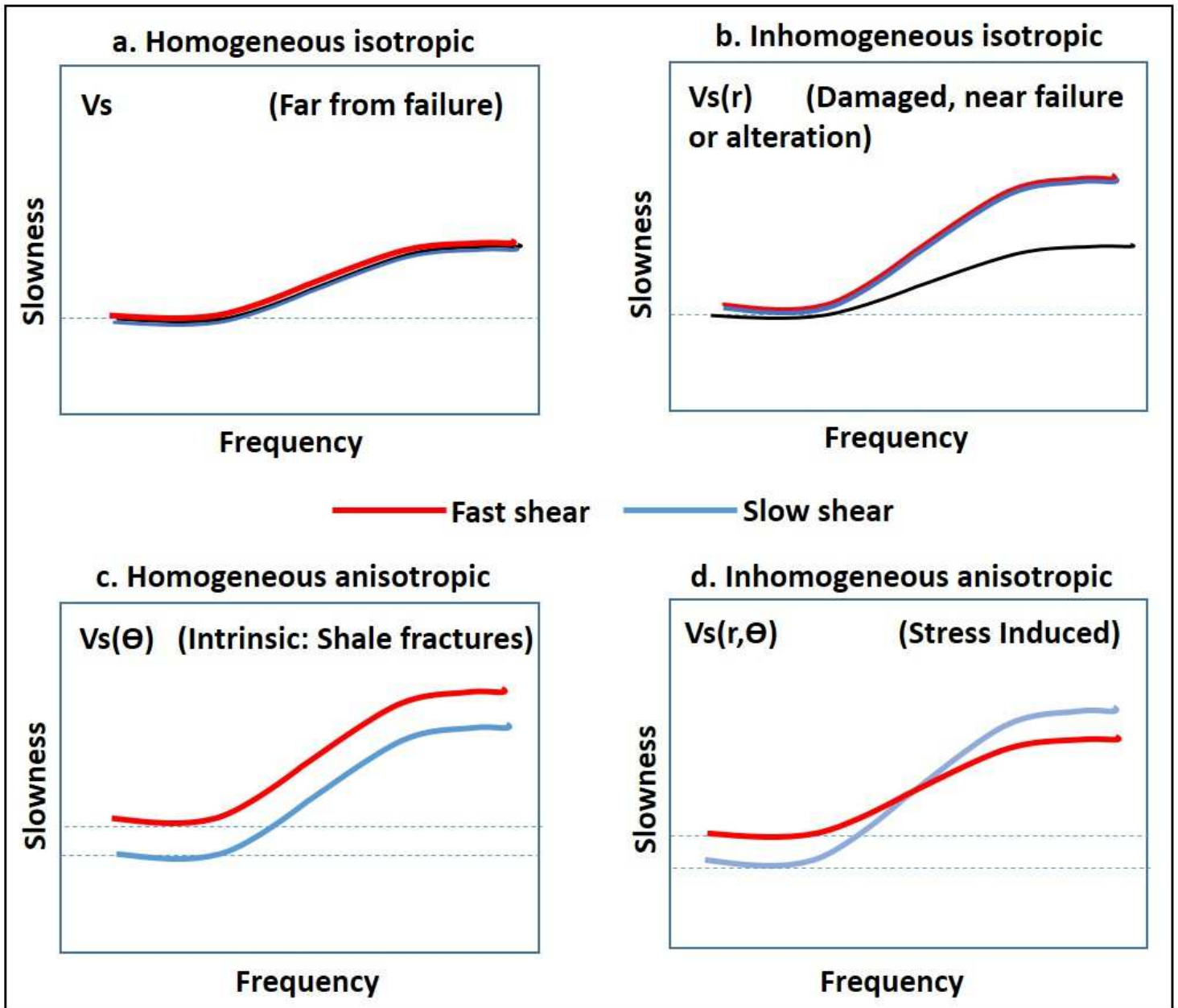


Figure 7

Classification of acoustic anisotropy from the fast shear (red line) and slow shear (blue line) wave in slowness versus frequency plot. (a) Homogeneous isotropic (b) Inhomogeneous isotropic (c) Homogeneous anisotropic (d) Inhomogeneous anisotropic (redrawn after Moreneo et al., 2013).

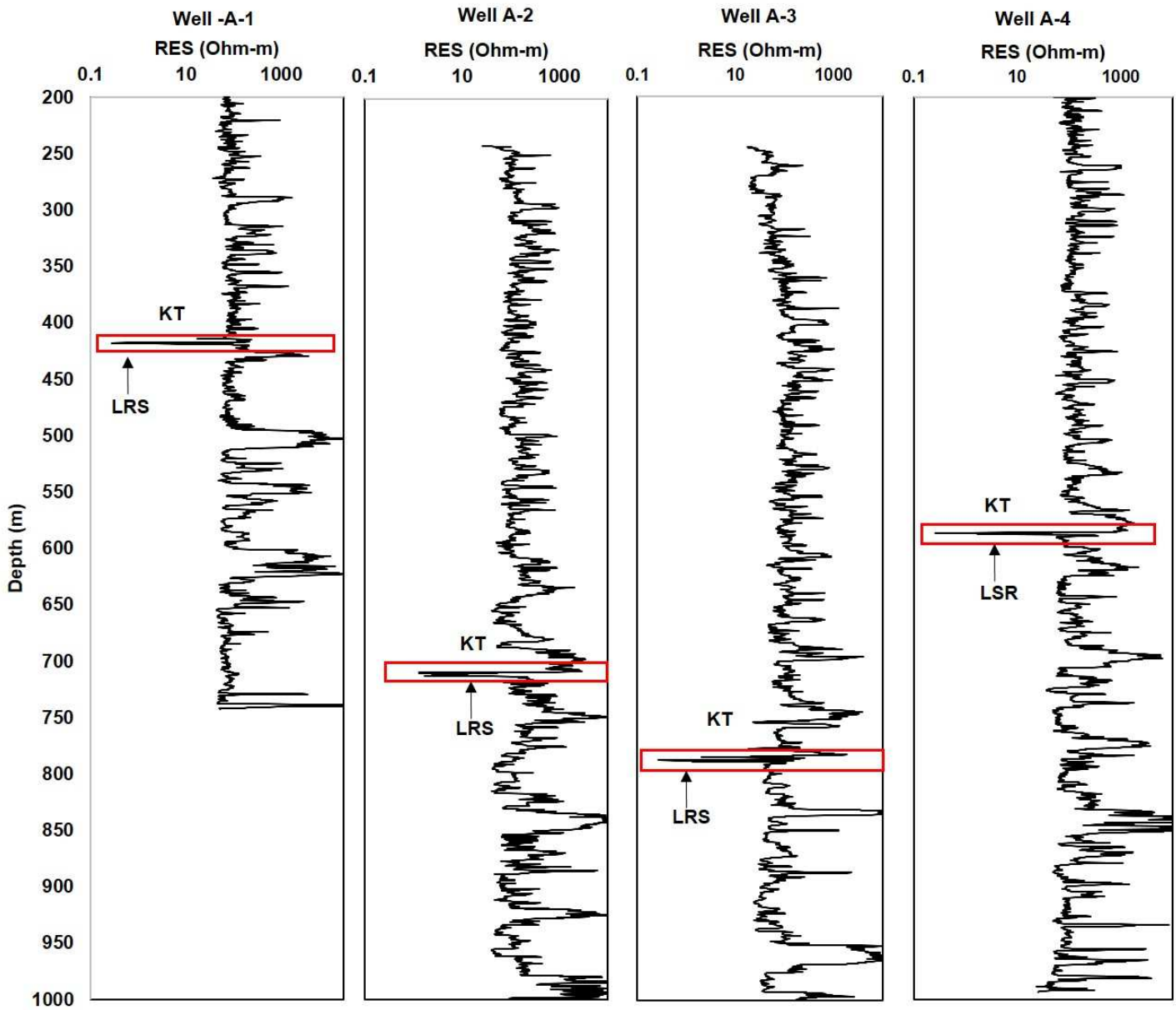


Figure 8

Correlation of low resistivity signature (LRS) shown in the red rectangular box below KT coal seam in the resistivity log of 04 wells (A-1, A-2, A-3, A-4).

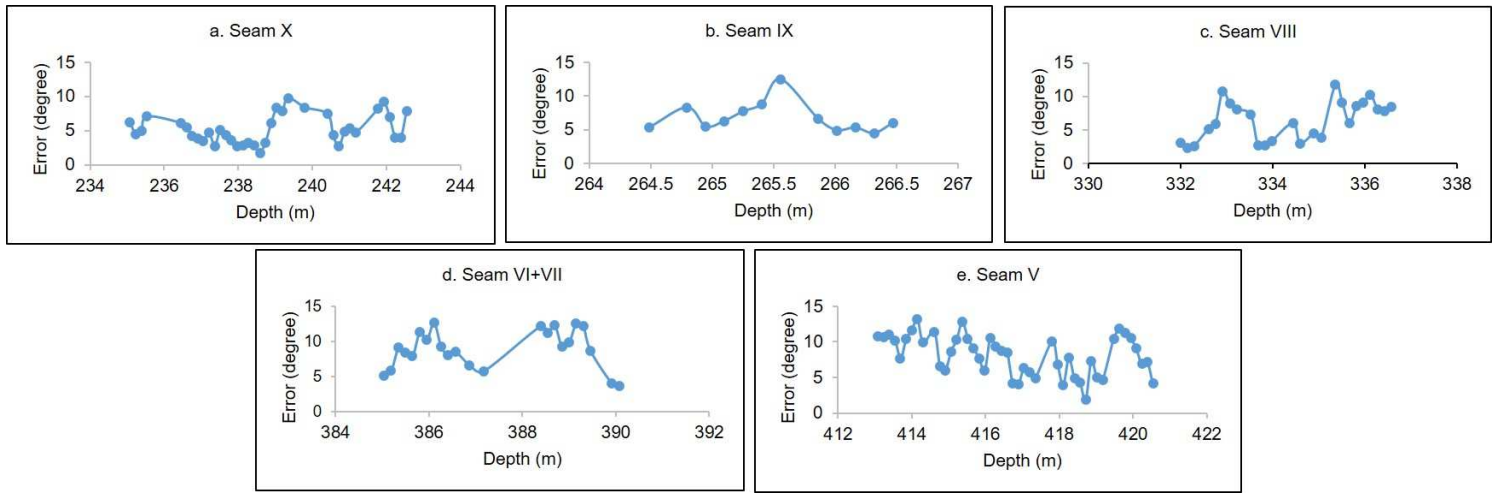


Figure 9

The error with depth point in (a) Seam-X (b) Seam-IX (c) Seam-VIII (d) Seam-VI+VII and (e) Seam-V.

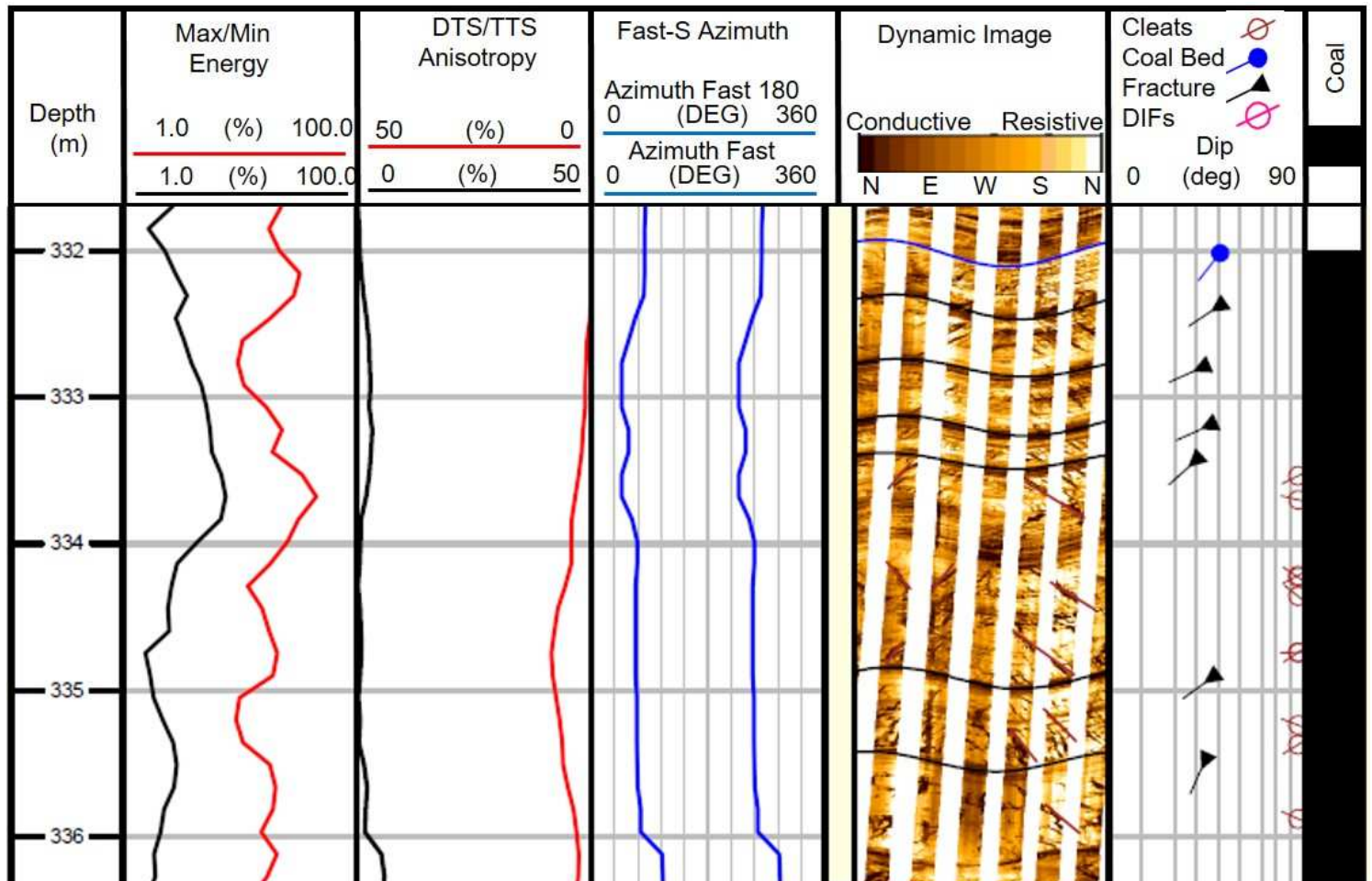


Figure 10

Anisotropy analysis representing seam-VIII in well W-2 illustrates maximum and minimum energy (%), DTS and TTS anisotropy (%), fast and 180° apart S-azimuth, resistivity image with dip.

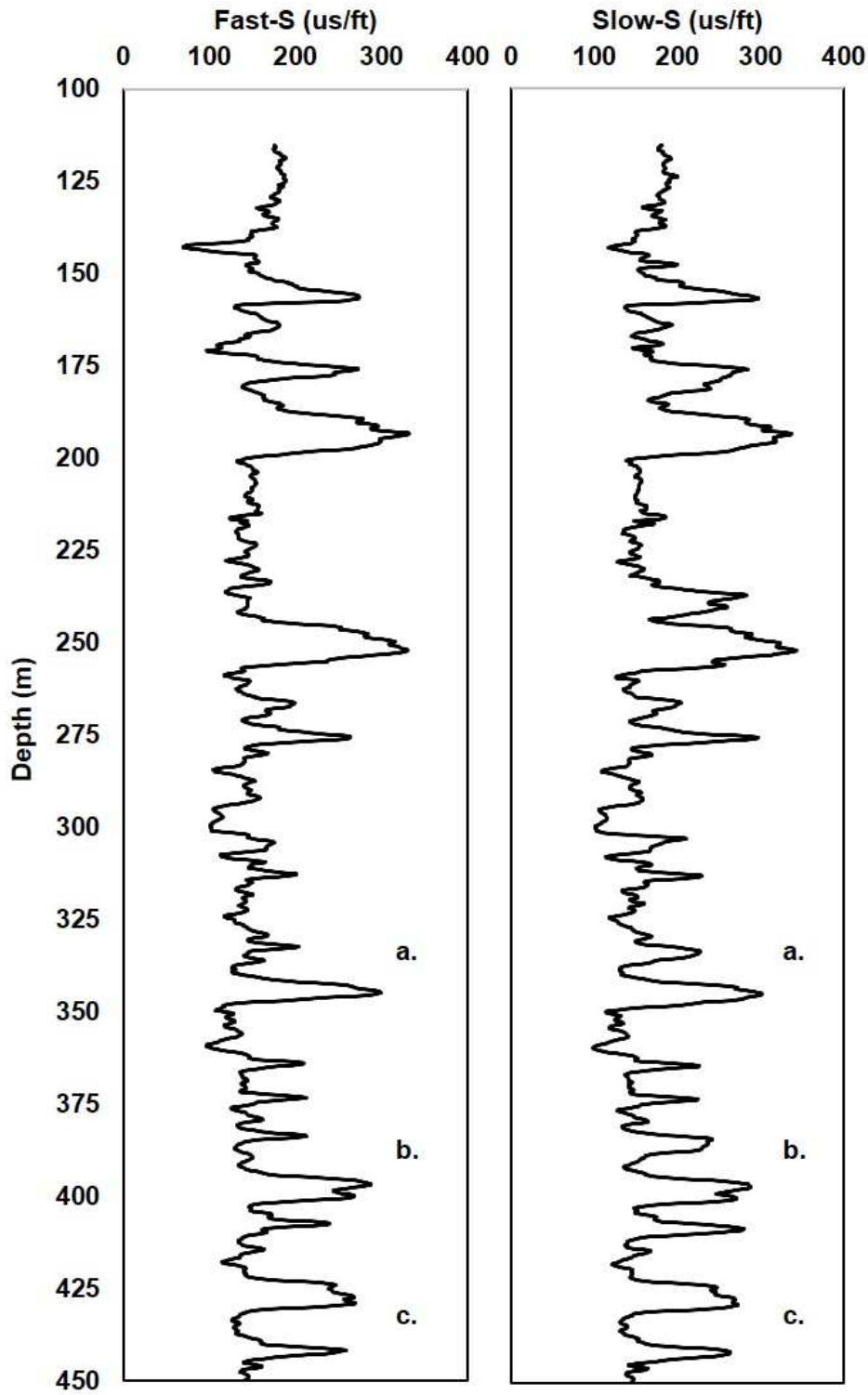


Figure 11

Fast and slow S-wave slowness (us/ft) from depth interval 115.0-450.0 m in well W-2 and 03 points (a, b, c) marked in the log for anisotropy characterization.

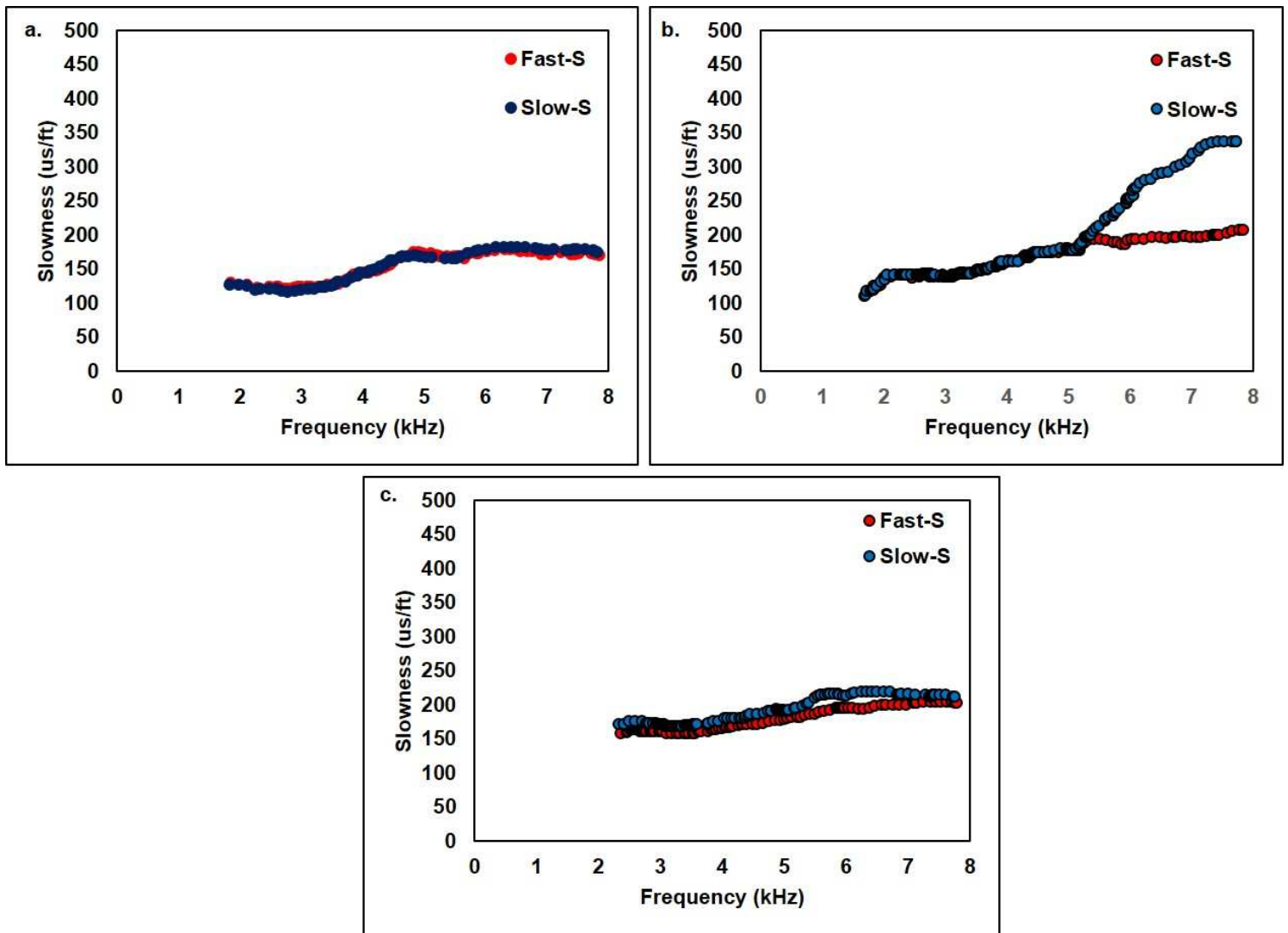


Figure 12

Slowness vs. frequency dispersion plot of fast (red) and slow (blue) S-wave at three depths: (a) Homogeneous isotropic formation at depth 342.0 m (b) Stress-induced fractured coal seam-V with inhomogeneous anisotropic characteristics at depth 389.0 m (c) Intrinsic anisotropy for homogeneous anisotropic formation at depth 437.0 m.

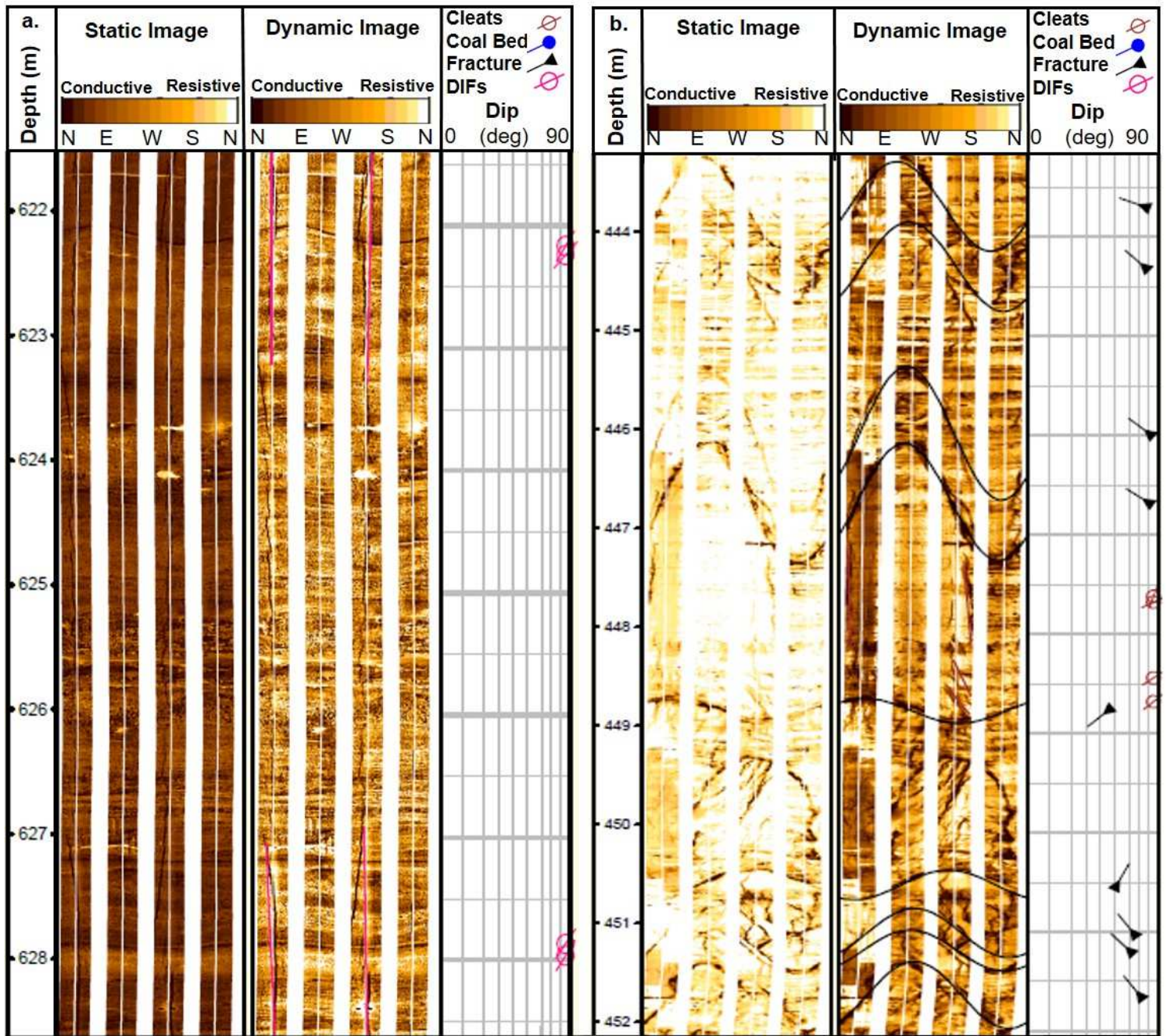


Figure 13

Static and dynamic resistivity image in well W-4 (a) represents DIFs with dip magnitude and direction from 622.0-628.0 m, (b) represents dip magnitude and direction of fractures and cleat in seam-V from depth interval 444.0-452.0 m.

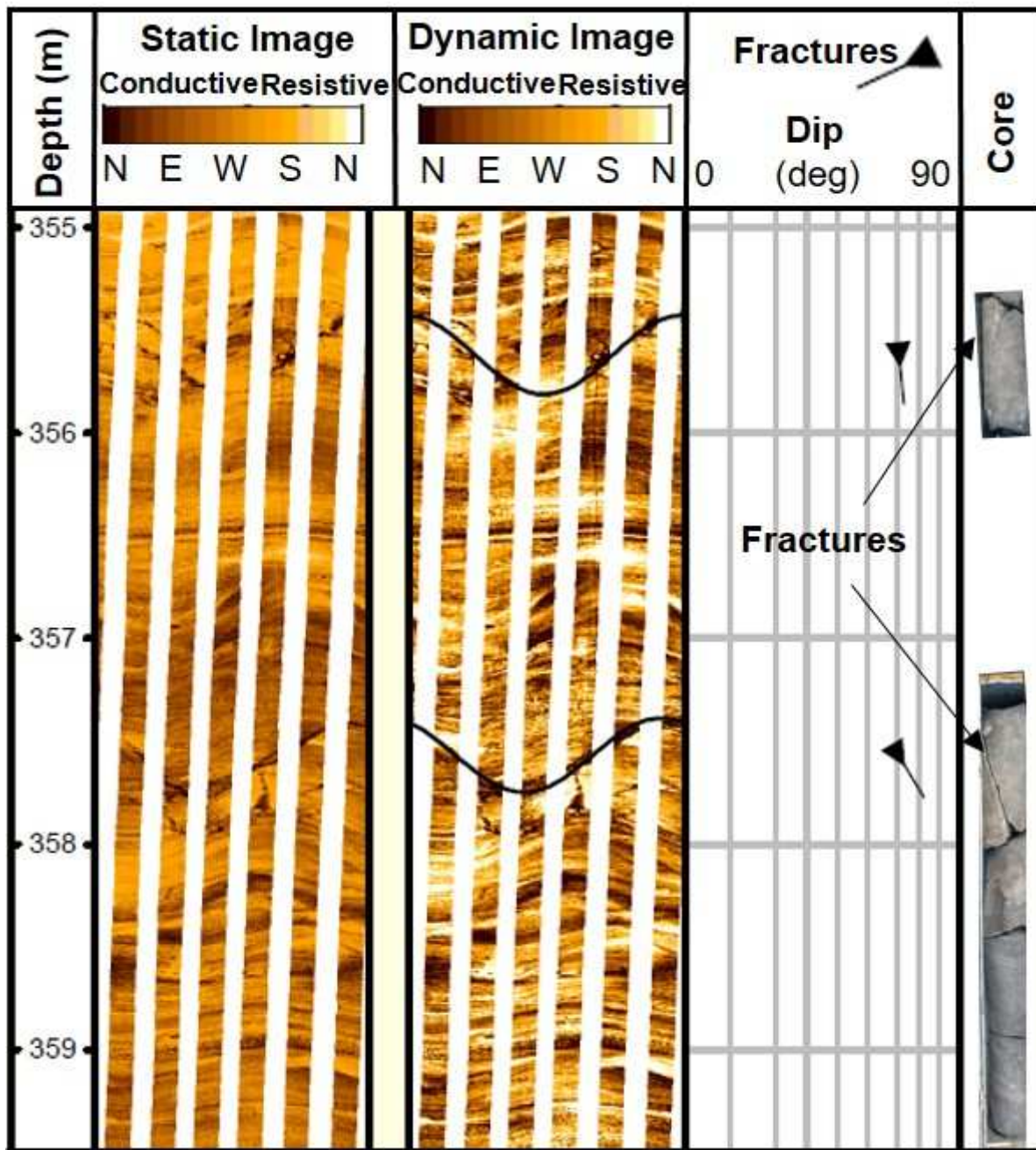


Figure 14

Correlation of fractures at 356.0 m and 357.5 m between drilling core and resistivity image log from depth 356.0 m to 362.5 m.

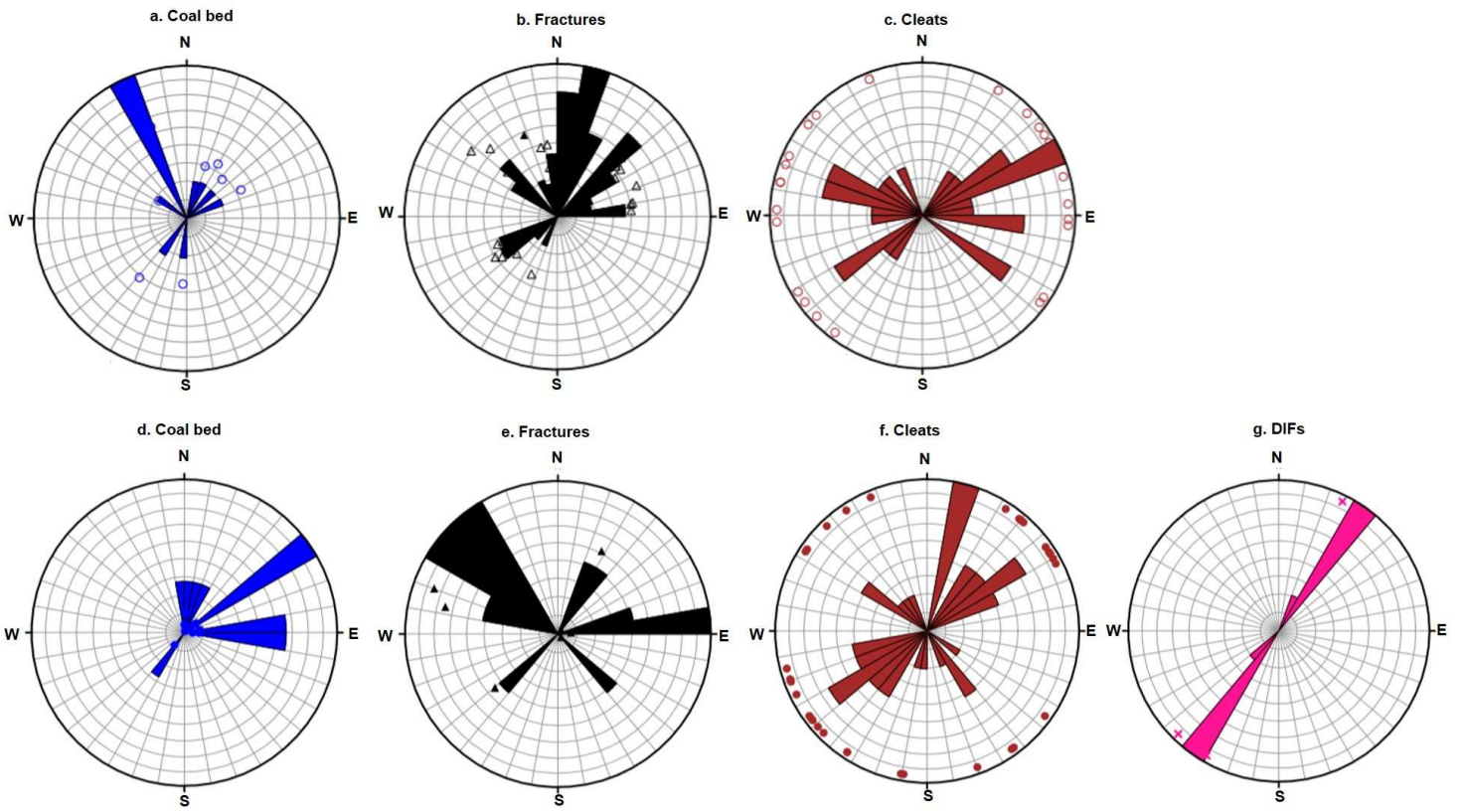


Figure 15

Stereonet plot representing dip magnitude and direction of 05 seams (V, VI+VII, VIII, IX, X) in well W-2 (a) fracture (b) cleats (c) coal bed; and in well W-4 (d) fracture (e) cleats (f) coal bed, (g) DIFs.

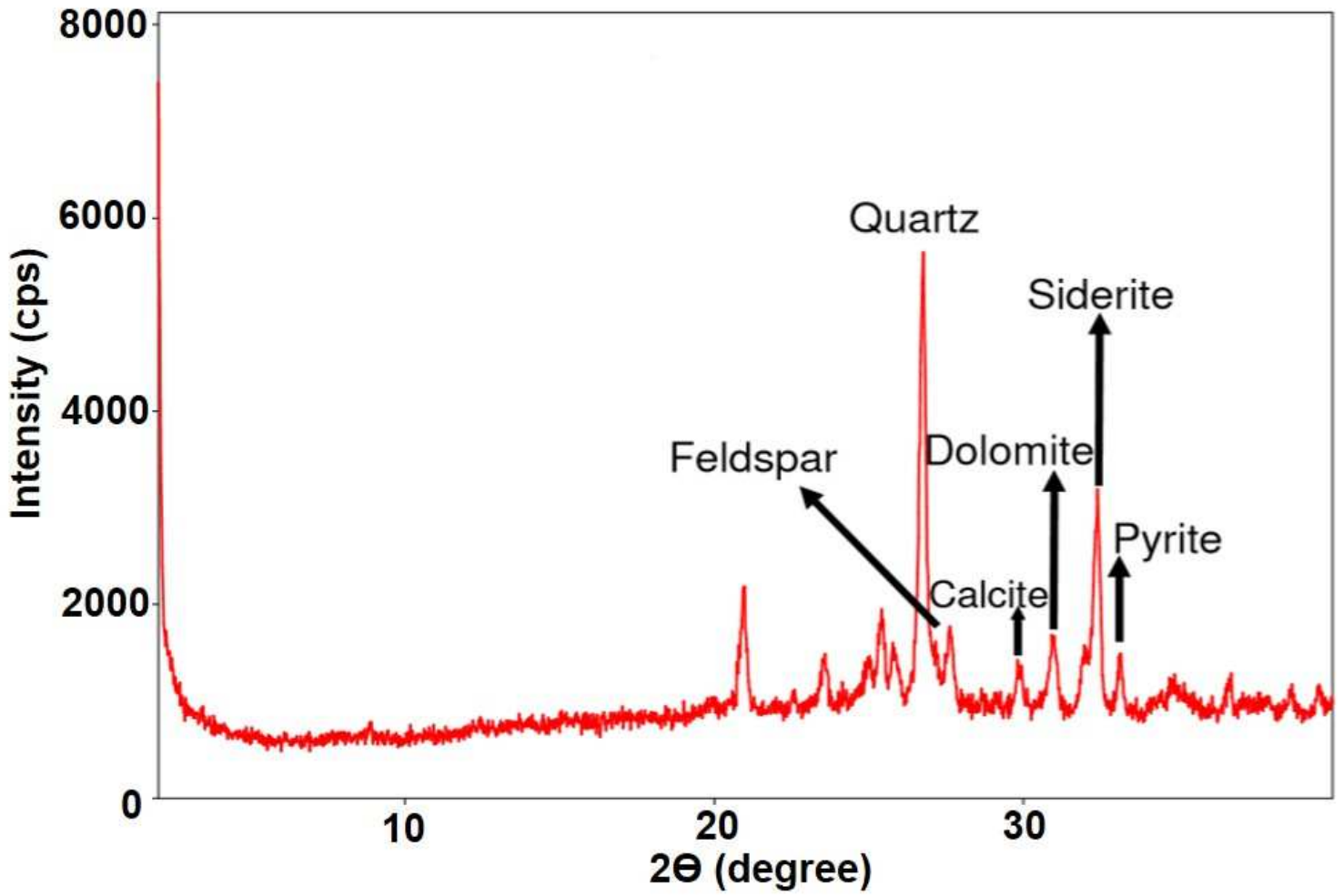


Figure 16

Cross-plot of intensity (cps) versus 2θ (degree) from the XRD studies of SWC at 418.0 m in well A-1 showing the presence of siderite and pyrite.